Russel E. Caflisch, Francesco Gargano,
Marco Sammartino and Vincenzo Sciacca

Complex singularities and PDEs

Abstract. In this paper we give a review on the computational methods used to capture and characterize the complex singularities developed by some relevant PDEs. We begin by reviewing the classical singularity tracking method and give an example of application using the Burgers equation as a case study. This method is based on the analysis of the Fourier spectrum of the solution and it allows to determine and characterize the complex singularity closest to the real domain. We then introduce other methods generally used to detect the hidden singularities. In particular we show some applications of the Padé approximation, of the Kida method, and of Borel-Polya method. We apply these techniques to the study of the singularity formation of some nonlinear dispersive and dissipative one dimensional PDE, of the 2D Prandtl equation and of the 2D Kadomtsev-Petviashvili equation. Finally the complex singularity analysis is applied to viscous high Reynolds number incompressible flows in the case of interaction with a rigid wall, and in the case of the vortex layers.

Contents

1 - Introduction

Many nonlinear partial differential equations (PDE) exhibit solutions that develop finite time singularities. Besides the intrinsic mathematical interest, to ask whether a PDE has a singular behavior is a crucial question because the occurrence of the singularity signals the limit of applicability of a PDE as mathematical model and often has physical significance. Therefore there is considerable interest in methods that can give indications whether a singularity is forming, where it is forming, and on its nature. In this review paper we shall focus on methods based on analytic continuation in the complex domain of numerical solutions of PDEs derived through spectral discretization.

The study in the complex plane of the analytic structure of the solutions of nonlinear PDE has in fact revealed to be a powerful method for the understanding of the process of singularity formation. The main idea behind the singularity tracking method [**69**] is to consider the analytic continuation of a function in the independent variable and to detect the width of the analyticity strip, i.e. the distance from the real domain to the nearest complex singularity. The width of the analyticity strip can vary with time and if a singularity reaches the real domain then the solution loses analyticity and becomes singular. The width of the analyticity strip can alternatively be bounded away from zero, or tend to zero asymptotically with time, in which case the solution develops increasingly small scales while remaining smooth.

The numerical implementation of this ideas typically involves high resolution (spectral) numerical computation of a time-evolution problem, while the location and other properties of the nearest complex singularity are determined from asymptotic behavior of the Fourier transform of the numerical solution. Indeed, the asymptotic properties of the Fourier transform for an analytic function of a single variable with isolated pole or branch point singularities at complex locations is determinate by the Laplace asymptotic formula, see [14] or [37]: more details on this and on the determination of the asymptotic behavior of the spectrum will be given in the next Section.

During the last three decades these ideas have been used extensively, particularly in the analysis of the (possible) singular behavior of flows and of PDEs arising in fluid dynamics. Examples include: the study of interface flow problems and of the singularity formation for vortex sheet equation [51, 52, 8, 20, 44, 66, 1, 59]; the investigation of the complex singularity formation for incompressible Euler flow; [11, 27, 58, 50, 16]; the analysis of the singularity formation for Prandtl solution and its connection to the separation phenomena [19, 21, 29, 30, 31]; as well the analysis of the singularity formation for Camassa-Holm and Degasperi-Procesi equations [21, 18], nonlinear Schrödinger equation [61], KdV [41], and others [41, 42].

When a PDE develops a finite time singularity the tracking of complex singularity gives valuable information on the time of blow up of the solution, on the spatial location and the algebraic character of the singularity. However, the method, as explained in [69] is able to characterize only the singularity closest to the real axis. In some cases it is also important to analyze other singularities in the complex plain. For example the analysis of the hidden complex singularities in [31] has revealed how the separation phenomena for the Navier Stokes equations is not related to the singularity of Prandtl equation.

To detect the hidden singularities one possibility is to use the Padé approximants. The advantage of the Padé approximation method is that it allows one to continue the function even beyond the radius of convergence (or strip of analyticity). Padé approximants also have been used in the analysis of complex singularities of various ordinary and partial differential equations, see [19, 31, 35]. Unfortunately information on the nature of the complex singularities are not so easy to compute using Padé approximants. For this reason, to detect the hidden complex singularities, new techniques have been recently introduced. The filtered method was introduced by Kida [40] while the method of Borel-Polya-Van der Hoeven has been proposed in [57]. Both methods are useful when one deals with a finite number of distinct complex singularities (poles or branches). We will discuss these methodologies in Section 3.

Another important implementation of the singularity tracking method is its extension to functions of several variables. If the singularity of a function of several

variables occurs along a single variable, a simple way to analyze the complex singularities is the application of the method of singularity tracking to this variable, see [**29, 21**]. In the more general case, it is possible to extend the singularity tracking method and detect complex singularity surface for a function of several variables from the full multidimensional Fourier transform. The main idea of this generalization consist to consider the analytic continuation in one variable and detect the complex singularity surface as a function of the other real variables. This analysis is based on the asymptotic properties of the multidimensional Fourier transform and in particular on the fact that the parameters, which characterize the singularity, are determined by the decay of the Fourier spectrum along or near a distinguished direction in wavenumber, which is the direction with the lowest decay rate. For example, one can see these applications in [**11, 10, 67, 58, 31, 48**].

The goal of the present paper is to give a brief review of some of the most recent advances in the singularity tracking method and to present some applications of interest in the field of fluid dynamics. Although most of the PDEs presented in this paper develop singularity in finite time and the numerical scheme used to solve them are suitable to capture these singularities, we mention that there is a very large literature devoted to theoretical and numerical methods used to avoid singularity formation. These methods depend on the nature of the PDE solved. For instance regularizing agents such as viscosity or regularized kernels are used to continue the vortex-sheet solution governed by the Birkhoff-Rott equation ([**2, 15**]) even beyond the singularity formation. Moreover numerical scheme using the $flux - limiter$ idea proposed originally by Van Leer in [**75**] are suitable for shock wave capturing in many hydrodynamics PDEs by limiting the solution gradients near shocks or discontinuities, and to produce high resolution schemes like the Monotonic Upstream-Centered Scheme for Conservation Laws or the Total Variation Diminishing without the spurious oscillations associated with some classical second order schemes (see [**76, 60, 36, 70, 56, 12**]). The term $slope - limiter$ is also used when limiting acts over system states as velocity or pressure.

The plan of the paper is the following. In Section 2 we present the method and we consider as an application, for the one dimensional case, the classical study of the singularity formation for Burgers equation. In Section 3 we present the methods to detect the hidden complex singularities: in Section 3.1 we discuss the Padé approximants theory, while the Kida method and the Borel-Polya-Van der Hoeven method are introduced in Section 3.2 and 3.3 respectively. These techniques are applied in Section 4 to several PDES. In Section 4.1 we investigate the complex singularities for the Kortweg de Vries equation and how they are related to the rapid oscillatory behavior of the solutions in the regime of small dispersion. In Section 4.2 we analyze the complex singularities of the wall shear of the Navier Stokes and

Prandtl equations and their relation with the mechanisms of unsteady separation phenomena. Finally in Section 5 we consider the singularity tracking method to analyze the complex singularities manifold for solutions of two dimensional PDEs; the applications presented are wall bounded flows at high Reynolds number and flows with highly concentrated vorticity in the form of a vortex layer.

2 - Complex singularity tracking

The complex singularity tracking method is based on the relationship between the asymptotic properties of the Fourier spectrum and the radius of analyticity of a real function.

Suppose that $u(z)$ is a real function analytic in the strip of the complex plane $\{z \in \mathbb{C} : |z| < \delta\}$. We suppose that the singularity closest to the real axis has complex location $z^* = x^* + i\delta$, and that $u(z) \sim (z - z^*)^\alpha$. Using a steepest descent argument it is possible to give the asymptotic (in k) behavior of the spectrum of $u(z)$:

$$(2.1) \qquad \hat{u}_k \sim C|k|^{-(1+\alpha)}\exp(-\delta|k|) \exp(ikx^*),$$

where with $\hat{u}_k$ we have denoted the Fourier coefficients.

Estimating the rate of exponential decay of the spectrum of the function u one gets the distance of the singularity from the real axis, the δ in (2.1). If one estimates the rate of algebraic decay (the α in (2.1)) one can characterize the singularity, and moreover the oscillatory behavior of the spectrum (the x^* in (2.1)) gives the location of the singularity. If the spectrum of the function u has not exponential decay, this means that the width of the strip of analyticity is zero and u has some kind of blow up. The estimate δ, α and x^* of (2.1) requires the use some fitting techniques (least square fitting for example), and in practical applications reveals to be a delicate matter.

We consider now a one dimensional evolutionary PDE

$$(2.2) \qquad u_t = F(u, u_x, u_{xx}, ...),$$

where $u = u(x, t)$, $x \in [0, 2\pi]$ is the spatial variable and $t > 0$ the time variable, and where with u_t and u_x, $u_{xx}, \ldots$ we denote the various partial derivatives of u with respect to t and x at different orders.

We discretize using Fourier-Galerkin spectral method and we transform the one dimensional PDE in a system of N ODEs

$$(2.3) \qquad \frac{d\hat{u}_k}{dt} = G_k(\hat{\boldsymbol{u}}), \qquad k = -N, \ldots, N,$$

where $\hat{\boldsymbol{u}} = (\hat{u}_k)_{|k|\leq N}$ and N is the order of the numerical truncation of the discrete Fourier series expansion

$$(2.4) \qquad u_N(x_j, t) = \sum_{k=-N}^{N} \hat{u}_k(t) \exp(ikx_j),$$

with $x_j = 2\pi j/N, j = 1, \ldots, N$.

Giving the initial condition to system (2.3) and solving numerically the ODE system (2.3) one can determine the time evolution of the Fourier spectrum $u_k(t)$. Studying the asymptotic behavior of the spectrum for large k gives the time evolution of the complex singularity, i.e. the path in the complex plane $(\delta(t), x^*(t))$ and the algebraic characterization $\alpha(t)$.

2.1 - *Application to one-dimensional PDEs*

Burgers equation is a good case study where to test the above ideas and in [**69**] the authors studied the shock formation process for the following problem:

$$(2.5) \qquad u_t + uu_x = 0, \qquad x \in [0, 2\pi],$$

with initial condition

$$(2.6) \qquad u(x, 0) = \sin(x),$$

and periodic boundary conditions.

From the classical results on the existence of classical solutions for conservation law (2.5) by the method of characteristic, the solution develops a singularity (a blow up on u_x) at time

$$(2.7) \qquad t_s = \frac{1}{-\inf_{x\in[0,2\pi]} u_x(x, 0)}.$$

The dynamics of the k-th Fourier mode of u is described by the following ODE

$$(2.8) \qquad \frac{d\hat{u}_k}{dt} = -\widehat{(uu_x)}_k.$$

To solve the above ODE system one can compute efficiently the nonlinear term through a pseudo spectral procedure, see e.g. [**7, 13**]; advancing in time can be achieved, e.g., using a 4th order explicit Runge-Kutta method. The process of progressive steepening of the wave until the blow-up of the spatial derivative can be observed in Fig. 1.

In Fig. 2 it is shown the behavior in time of the spectrum of the solution starting at time $t = 0.6$ up to singularity time $t_S = 1$.
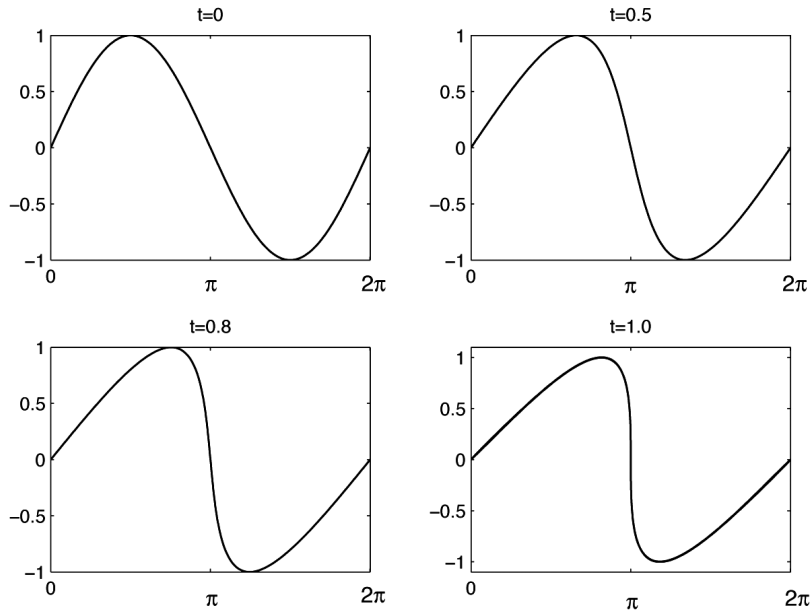
Fig. 1. The behavior in time of the numerical solution of Burgers equation with initial condition (2.6). At time $t_S = 1$ one can see a singularity as a blow up of the first derivative.
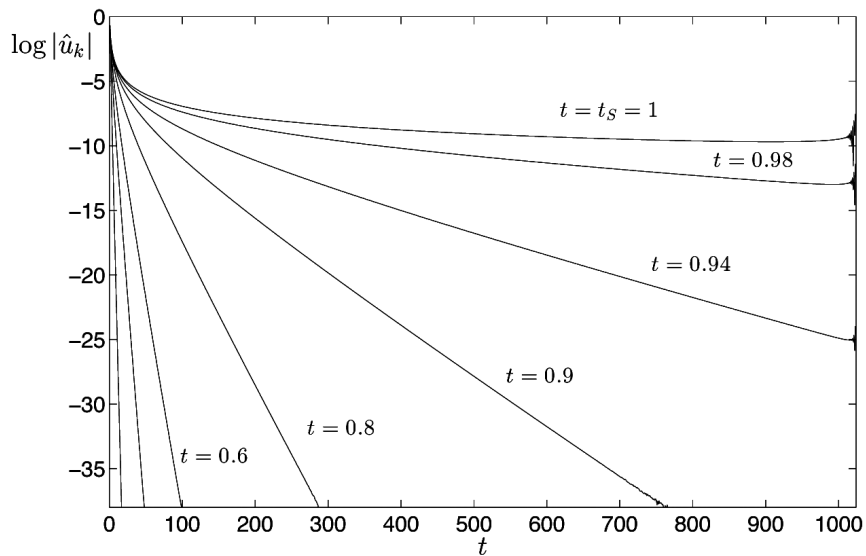
Fig. 2. The behavior of the spectrum in time of the Burgers equation numerical solution with initial datum (2.6), starting at time $t = 0.6$ up to singularity time $t_S = 1$.
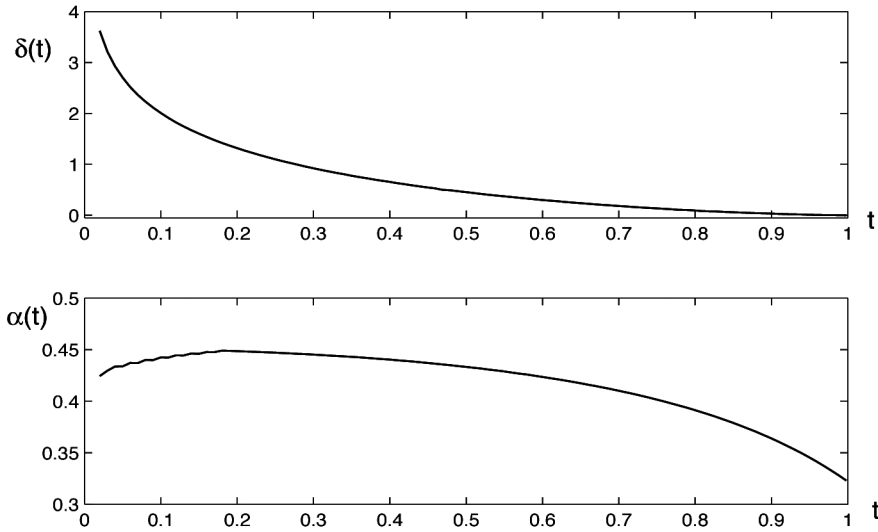
Fig. 3. The tracking singularity method applied to Burgers equation numerical solution with initial datum (2.6). In the top, the behavior in time of the width of the analyticity strip δ. In the bottom, the behavior in time of the algebraic character α. The singularity time is $t_S = 1$. The singularity is of cubic–root type.

For symmetry reasons one has that a complex singularity comes with its complex conjugate. Therefore the asymptotic formula (2.1) in this case becomes:

$$(2.9) \qquad \hat{u}_k \sim C|k|^{-(1+\alpha)}\exp(-\delta|k|)\cos(kx^*).$$

In this case a simple least square fitting procedure applied to the numerical data of the spectrum is able to give the values of the parameters δ, x^* and α of (2.9). The results are shown in Fig. 3. The critical time t_S where $\delta(t_S) = 0$ is the singularity time $t_S = 1$ and the singularity algebraic character $\alpha(t_S)$ is of cubic–root type. One can also notice from Fig. 4 that the location of the singularity is in $x^* = \pi$.

The above numerical results are in perfect agreement with the findings of Fournier and Frisch obtained in [26] using asymptotic analysis techniques in the study of the Fourier-Lagrange modes. In fact they showed that the solution of the above problem has two complex conjugate singularities of square–root type located in $\pi \pm i\delta(t)$ which collide, at time $t = t_S = 1$, at $x^* = \pi$ and $\delta = 0$ to form a real cube-roots singularity.

Other fitting procedure can certainly be used, see [6] for a discussions on the issues related to the fitting procedures. Here we mention that in [41] the fitting procedure was based on the minimizing the L^∞ norm

$$(2.10) \qquad \Delta = \|\log|\hat{u}_k| - (C - (1 + \alpha)\log|k| - \delta k)\|_\infty.$$
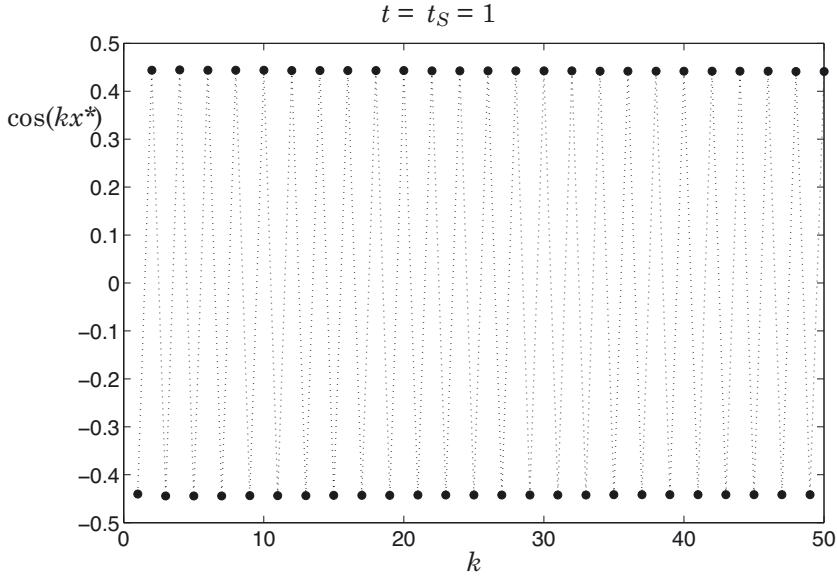
$$t = \ t_S = 1$$

Fig. 4. The tracking singularity method applied to Burgers equation numerical solution with initial datum (2.6). The behavior in k of the term $\cos(kx^*)$ in formula (2.9), at the singularity time $t_S = 1$.

A different analysis of the singularity formation can be performed with the so called sliding–fitting technique with length 3, see [**11, 21, 58, 66**] for details. This procedure consists in searching the values of C, α and δ of the asymptotic formula (2.1) locally to each k mode, using only the $(k-1)$-th, k–th and $(k+1)$-th modes of the spectrum. The formulas are:

$$(2.11) \qquad \alpha(k) = \frac{\log\left(\dfrac{\hat{u}_{k-1}\hat{u}_{k+1}}{\hat{u}_k^2}\right)}{\log\left(\dfrac{k^2}{(k-1)(k+1)}\right)},$$

$$(2.12) \qquad \delta(k) = \left[\log\left(\frac{\hat{u}_k}{\hat{u}_{k+1}}\right) + \alpha \log\left(\frac{k}{k+1}\right)\right],$$

$$(2.13) \qquad \log C(k) = \log|\hat{u}_k| + \alpha(k)\log(k) + k\delta(k).$$

These values depend on k, and the asymptotics can be computed with an extrapolation process using the epsilon algorithm of Wynn, see [**11, 58**]. The results of

the sliding fitting procedure with length 3, are shown in Fig. 5 for the Burgers equation.

Another techniques is the Van der Hoeven asymptotic interpolation method, recently discussed in [57]. An important feature of the asymptotic interpolation method is that it uses the determination of subleading terms to improve the accuracy on leading order terms. We now explain this method and we refer to [57, 31] for applications of this technique.

Suppose the following asymptotic expansion on the spectrum holds:

$$(2.14) \qquad \hat{u}_k \sim C \frac{1}{k^{\alpha+1}} e^{-\delta k} \left(1 + \frac{\gamma_1}{k} + \frac{\gamma_2}{k^2} + \frac{\gamma_3}{k^3} + O(k^{-4}) \right).$$

We apply successively the following six transformations to identify the parameters C, α, δ, γ_1, γ_2, γ_3:

$$\hat{u}_k \to SR(\hat{u}_k) = \hat{u}_k^{(1)} \to -D(\hat{u}_k^{(1)}) = \hat{u}_k^{(2)} \to I(\hat{u}_k^{(2)}) = \hat{u}_k^{(3)}$$

$$(2.15) \qquad \to D(\hat{u}_k^{(3)}) = \hat{u}_k^{(4)} \to D(\hat{u}_k^{(4)}) = \hat{u}_k^{(5)} \to D(\hat{u}_k^{(5)}) = \hat{u}_k^{(6)},$$
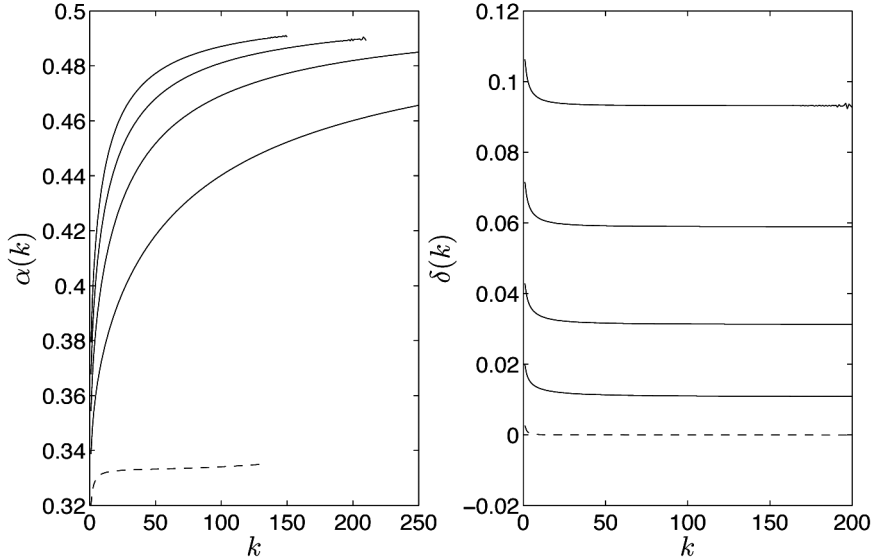

Fig. 5. The sliding fitting procedure of length 3 for the Burgers equation with initial datum (2.6). On the right (left) figure the $\alpha(k)$ ($\delta(k)$) behaviors w.r.t. k, starting at time $t = 0.8$ up to singularity time $t_S = 1$ with increments of 0.05 (the dashed lines correspond to the singularity time).

where

$$I : U_k \to \frac{1}{U_k}$$

$$R : U_k \to \frac{U_k}{U_{k-1}}$$

$$SR : U_k \to \frac{U_k U_{k-2}}{U_{k-1}^2}$$

$$D : U_k \to U_k - U_{k-1}.$$

The last term $\hat{u}_k^{(6)} = 3/(\alpha + 1)$ is a constant which is easy to identify. Inverting the chain (2.15), one can find the values of the parameters in (2.14). This is the sixth stage procedure and in Table 1 we give the results for the Burgers equation. As explained in [57], it is possible to consider other parameters in the asymptotic formula (2.14) which can be identified using more stages.

The asymptotic interpolation method is best computed using high digit precision computation. In [57] the authors perform a six stages procedure with 80-digit precision (and the 13-stage procedure with 120-digit precision) obtaining data with accuracy of the order of 10^{-7}. Here we have performed the six stage procedure in double precision and we note that the coefficients C, α and δ have accuracy of the order of 10^{-4}, while the coefficients γ_1, γ_2 and γ_3 have worst accuracy.

Table 1. *The results at different times for Burgers equation of the Van der Hoeven asymptotic interpolation method applied to* (2.14), *using the six stage procedure* (2.15).

	$t = 0.8$	$t = 0.85$	$t = 0.9$	$t = 0.95$	$t = t_S = 1$
C	0.70713615783	0.61442246421	0.51993097752	0.43513434016	0.47175434493
α	0.49965144521	0.49948664577	0.49612632902	0.49624364601	0.33296382179
δ	0.09606920975	0.05363644145	0.01544724997	0.00331071154	± 0.00000355044
γ_1	-1.47272447227	-1.8634299638	-2.4808780250	-5.63365314047	-0.66772591307
γ_2	1.96722910228	6.19701488066	13.37505045755	89.95119911733	-0.12956190944
γ_3	13.10231991191	34.55734201601	58.35449497230	81.24726572859	-83.44565528569

Formulas (2.11)-(2.13) for the sliding fitting, or the Van der Hoeven asymptotic interpolation method, are useful when the spectrum does not have oscillatory behavior, like in the case of Burgers equation considered.

In other case when $x^* \neq \pi$, one can fit $L + 1$ modes of the spectrum starting from a certain $\hat{u}_k$, i.e. the set $\{\hat{u}_k, ..., \hat{u}_{k+L}\}$, using again a least square fitting method. This way one determines certain $\delta_L(k)$ and $\alpha_L(k)$ that, if relatively independent from L and k (at least in the central part of the spectrum), give reliable information on the location and on the nature of the singularity. This technique is applied in [18, 21] for the investigation on the blow up for the Camassa-Holm and the b-family equations.

3 - Hidden complex singularities

As we have seen in the previous section, the method of complex singularity tracking is useful to study the blow up phenomena of an evolutionary PDE. However the method gives information only to the complex singularity closest to the real axis. Often it is also important to analyze the other singularities in the complex plain. In this section we present some techniques that can reveal the presence of complex singularities that, being more distant from the real axis, are hidden by the main (the closest to the real axis) complex singularity.

Application of the various methods presented here will be given in Section 4.

3.1 - *Padé analysis*

In this section we recall the Padé approximations.

Suppose there is a complex function $f(z)$ expressed by a power series $f(z) = \sum_{k=0}^{\infty} f_i z^k$, the Padé approximant $P_{L/M}$ is a rational function approximating f, such that

$$(3.1) \qquad f(z) \approx \frac{\sum_{i=0}^{L} a_i z^i}{1 + \sum_{j=1}^{M} b_j z^j} = P_{L/M}(z),$$

with the property that

$$(3.2) \qquad f(z) - P_{L/M}(z) = O(z^{L+M+1}),$$

where $L + 1$ and M are the number of coefficients in the numerator and denominator respectively.

The M unknown denominator coefficients $b_j, j = 1 \ldots, M$ and the $L + 1$ unknown, $a_i, i = 0, \ldots, L$ are determined uniquely by (3.2) equating coefficients of equal powers of z between $(\sum_{i=0}^{\infty} f_i z^i)(1 + \sum_{j=1}^{M} b_j z^j)$ and $\sum_{i=0}^{L} a_i z^i$, setting the coefficients of order greater than L equal to zero, and $b_0 = 1$ by definition. The following set of M linear equations must be solved

$$(3.3) \qquad \begin{aligned} b_M f_{L-M+1} + b_{M-1} + \ldots + b_0 f_{L+1} &= 0, \\ &\vdots \\ b_M f_L + b_{M-1} f_{L+1} + \ldots + b_0 f_{L+M} &= 0. \end{aligned}$$

Then the $L+1$ unknown numerator coefficients $a_i, i = 0, \ldots, L$ follow from $(\sum_{i=0}^{\infty} f_i z^i)(1 + \sum_{j=1}^{M} b_j z^j) = \sum_{i=0}^{L} a_i z^i$ by equating coefficients of equal powers of z less then or equal to L.

It is possible to use Padé approximants for Fourier series [**4, 77**]. Consider

$$(3.4) \qquad u(x) \approx \sum_{k=-N}^{N} \hat{u}_k e^{ikx},$$

an approximate solution to a PDE at a specific time t. If we denote by $z_+ = e^{ix}$ and $z_- = e^{-ix}$, the Fourier series on the right may be expressed as the sum of two power series in the complex variables z_+ and z_-:

$$(3.5) \qquad u(x) \approx \sum_{k=0}^{N} \hat{u}_k z_+ + \sum_{k=0}^{N} \hat{u}_k z_- - \hat{u}_0.$$

Both power series on the right may now be converted to Padé approximants

$$(3.6) \qquad u(z) \approx P_{L/M}(z_+) + Q_{L/M}(z_-) - \hat{u}_0,$$

with $L + M + 1 = N$.

The advantage of the Padé approximation method is that it allows one to continue the function f even beyond the radius of convergence (or strip of analyticity), although convergence issues can arise near branch points or branch cuts. The disadvantage of the Padé approximation method is that not all of the singularities represented by a general $P_{L/M}$ are singularities of the function being approximated.

In fact, there are several examples (see, for example, [**4**]) for which some defects or spurious singularities can appear. However, these defects can in principle be detected as the spurious singularities generally manifest as a pole very close to the zeros of $P_{L/M}$. Moreover these spurious singularities have a transient nature as they usually disappear by changing the degrees of the Padé approximation. Another issue is represented by the fact that the linear system (3.3) is close to being singular (ill-conditioned), particularly when one seeks a high degree Padé approximant. To overcome these problems one possibility is to compute function values of $P_{L/M}(z)$ for a given z. This technique may be done efficiently using Wynn's epsilon algorithm, and we refer to [**4**] for the details. A different possibility instead is to use high numerical precision computation: in this paper we shall focus on this technique.

If the singularities are poles it is easy to locate and characterize the singularities. If we have the explicit expression of $P_{L/M}$ (found by solving the linear system (3.3))

one can simply compute the roots of the denominator of $P_{L/M}$. Moreover, the algebraic character of the poles is the algebraic multiplicity of the roots. On the other hand, if one has computed numerically the values of Padé approximants on given points z it is possible to find the poles searching the maximum of the following function:

$$(3.7) \qquad\qquad f(z) = \log |u(z)|.$$

Instead, to compute the order of the pole, it is possible to use the argument principle [77]:

$$(3.8) \qquad\qquad \frac{1}{2\pi i} \int\limits_C \frac{u'(z)}{u(z)} dz = Z(u) - P(u),$$

where C is a closed curve (for computational reasons it is possible to choose C as the circle centered in the poles location) and where $Z(u)$ is the number of zeros and $P(u)$ is the number of poles (counting multiplicity) of u inside C. As it is known, if u is analytic and nonzero at each point of a simple closed positively oriented contour C, and inside C the only singularities of u are poles, if C is chosen very close to the poles then $Z(u) = 0$ and $P(u)$ determines the algebraic order of the pole singularity. If the singularity is an algebraic branch points or other type of singularity like logarithmic branch points or essential singularities, the singularity appears as a string of poles and zeros located along the branch cut (see [4, 77]).

Padé approximants also have been used in the analysis of complex singularities of various ordinary differential equations (see [19, 31, 35]). The theoretical and practical issues related to Padé-based methods are so numerous that it is impossible to cite them all here, and the reader is referred to [4] and [35] for a good discussion of this topic.

In the rest of this paper we shall see several instances where the Padé approximants are an effective tool to detect singularities which are outside the strip of analyticity of a Fourier series. Here we present as an example, the Padé approximants of the solution of the inviscid Burgers equation (2.5) with initial datum (2.6). We compute the coefficients of the Padé approximant $P_{L/M}$, with $M = L = 50$, solving the algebraic system (3.3) and considering the Fourier coefficients of the numerical solution of Burgers equation. In Fig. 6 it is shown the absolute value, at different times, of the analytic continuation $P_{L/M}(z)$ in the complex plane of the solution of Burgers equation. As we said in Section 2, the solution has two square root singularities, placed symmetrically on the imaginary axis with respect to the origin. These singularities move from infinity at the initial time toward the real axis, where they meet at the singularity time $t_S = 1$. The singularities of $P_{L/M}(z)$ appears in
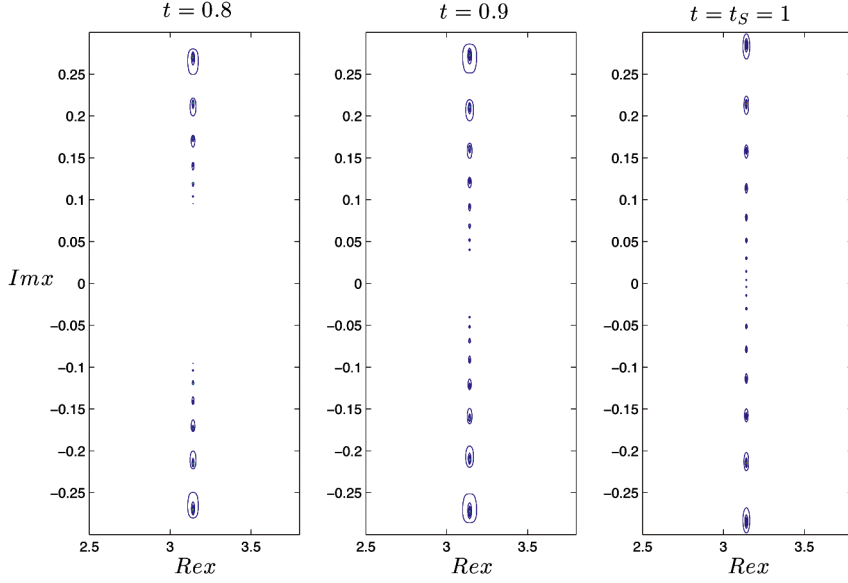
Fig. 6. Inviscid branch point and branch cuts at different times for the inviscid Burgers equation.

Fig. 6 as a string of poles located at the corresponding branch cut which is the imaginary axis. The singularities approach the real axis according to the results of the singularity tracking method in Fig. 3.

3.2 - *Kida technique*

The method introduced by Kida in [**40**] consists in filtering the function $u(x)$ with

$$(3.9) \qquad v(x|X,d) = u(x)G(x|X,d),$$

where $G(x|X,d)$ is a Gaussian-type filtering function which as a peak in $x = X$ with standard deviation d:

$$(3.10) \qquad G(x|X,d) = \frac{1}{d\sqrt{\pi}}\exp\left[-\frac{(x-X)^2}{d^2}\right].$$

Taking the Fourier transform

$$(3.11) \qquad \hat{v}(k|X,d) = 2\pi \int_{-\infty}^{\infty} \hat{u}(\xi)\hat{G}(k-\xi|X,d)d\xi,$$

with

$$\hat{G}(k|X,d) = \exp\left[-\frac{k^2 d^2}{4} + ikX\right],$$ (3.12)

and using the Laplace asymptotic formula (2.1) to the previous relation one has:

$$\hat{v}(k|X,d) \sim \sum_j A_j |k|^{-\alpha_j - 1} \exp\left[ikz_j - \frac{(X - z_j)^2}{d^2}\right],$$ (3.13)

while the exponential decay is given by

$$\Delta_j(k|X,d) = -\delta_j k - \frac{-(X - x_j^*)^2 - \delta_j^2}{d^2}$$ (3.14)

where $z_j = x_j^* + i\delta_j$ are the complex singularities.

Note that $\Delta_j(k|X,d)$ is larger for x_j^* closer to X or for smaller δ_j as long as $k \leq \delta_j/d^2$.

If one denotes by $j = J$ the term which gives the maximum of $\Delta_j(k|X,d)$ over a certain range of k, then the previous formula can be approximate by

$$\hat{v}(k|X,d) \sim A_J |k|^{-\alpha_J - 1} \exp(-k\delta_J),$$ (3.15)

which decrease exponentially in k. One can therefore estimate the δ of the most relevant singularities which exist within distance d from X, by estimating the exponential decay rate of the spectrum.

3.3 - *Borel-Polya-Van der Hoeven method*

In this section we review the Borel-Polya-Van der Hoeven method (BPH method in the sequel) proposed in [57] to retrieve more information about the singularities outside the width of the analyticity strip of the Burgers equation for different initial conditions. This method is useful when one deals with a finite number of distinct complex singularities (poles or branches).

In particular, given the inverse Taylor series $f(z) = \sum_{k=0}^{N} f_k/z^{k+1}$ that has n complex singularities $c_j = |c_j| e^{-i\gamma_j}$ for $j = 1, 2, \ldots, n$, its Borel transform is given by $U_B(\zeta) = \sum_{k=0}^{N} f_k \zeta^k/n!$. Evaluating the modulus of the Borel series $G(r) = |U_B(re^{i\phi})|$ along the rays $re^{i\phi}$, one obtains, through a steepest descent argument, the following asymptotic behavior

$$G(r) \approx C(\phi) r^{-(\alpha(\phi)+1)} e^{h(\phi)r} \quad \text{for} \quad r \to \infty.$$ (3.16)

The function $h(\phi)$ is called the *indicatrix* function of the Borel transform. To better understand the role of the indicatrix function, we consider the set $K = \{c_1, \ldots, c_n\}$ of

all the singularities, and we define the *supporting line* of K as a line that has at least one point in common with K and such that its points are in the same half space with respect to the supporting line of K. The intersection of all these half spaces is the *convex hull* of K, which in the case of separate poles or branches reduces to the smallest convex polygon containing all the singularities as illustrated in Figure 7. The *supporting* function $k(\phi) = h(-\phi)$ is the distance from the origin to the supporting line normal to ϕ. In [57], it has been shown that, in the case of isolated singularities, the indicatrix function is the piecewise cosine function

$$(3.17) \qquad h(\phi) = |c_j| \cos(\phi - \gamma_j) \quad \text{for} \quad \phi_{j-1} < \phi < \phi_j,$$

where the angular intervals (ϕ_j, ϕ_{j+1}) are depending on the complex positions of the singularities (we refer to [57] for a deeper explanation on how the set ϕ_j, $j = 1, 2, \ldots, n$ is determined). Therefore, through numerical interpolation we can determine the parameters $|c_j|$ and γ_j that give the locations of the complex singularities c_j. In practice, for each direction ϕ we need to determine the exponential rate of (3.16) that allows for construction of the indicatrix function h. Moreover, an es-
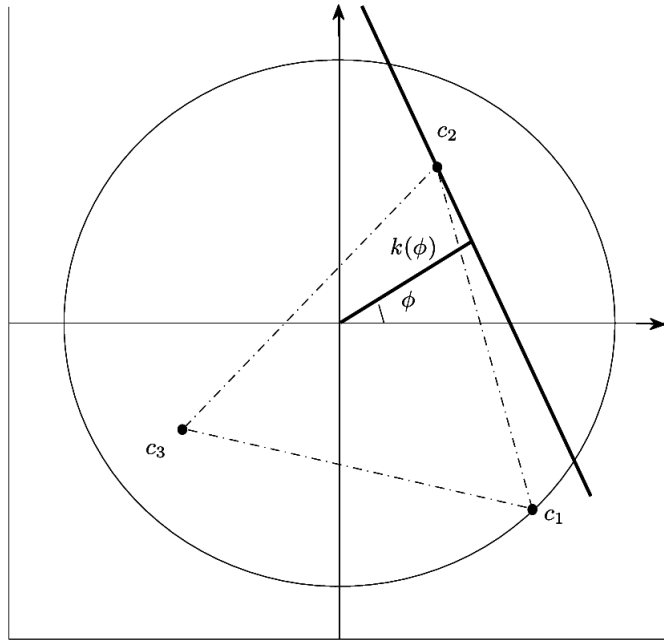

Fig. 7. The convex hull of a discrete set of complex singularities is the smallest convex polygon containing all the singularities c_i. The *supporting* function $k(\phi)$ is the distance from the origin to the supporting line, normal to the direction ϕ, and touching a singularity.

timate of $\alpha(\gamma_j)$ in (3.16) returns the characterization of the singularity c_j. The BPH method can be easily applied to the Fourier series $f(z) = \sum_{k=-K/2}^{k=K/2} f_k e^{ikz}$ by introducing the complex variables $Z_+ = e^{iz}, Z_- = e^{-iz}$ so that

$$(3.18) \qquad u(z) = \sum_{k=0}^{K/2} u_k e^{ikz} + \sum_{k=1}^{K/2} u_k e^{-ikz} = \sum_{k=0}^{K/2} u_k / Z_-^k + \sum_{K=1}^{K/2} u_k / Z_+^k.$$

The advantage of this methodology in comparison to the singularity-tracking method lies in the fact that it is possible to capture information on the singularities located outside the radius of convergence of a Taylor series (or the strip of analyticity of a Fourier series). However, there are some drawbacks. In particular, singularities that are close to each other can be difficult to distinguish, mainly because a cosine function relative to a singularity s_1 can be *hidden* by another cosine function relative to a singularity s_2, if s_2 is closer to the real domain than s_1. Using high numerical precision in conjunction with the asymptotic extrapolation method proposed in [73] can only in part overcome this issue. Moreover, the computational cost is heavier in comparison to the singularity-tracking method, as a numerical interpolation must be performed in various directions containing all of the singularities.

4 - Applications

4.1 - *Dispersion and dissipation*

In this section we shall apply the techniques explained in the previous sections to analyze the complex singularities of some nonlinear dissipative and nonlinear dispersive PDEs. Many nonlinear dispersive systems, in the regime of small dispersion, exhibit rapid oscillations in their spatio-temporal dependence. Although a fascinating mathematical phenomenon, these oscillations are generally quite difficult to describe and control and are an obstacle to the efficiency of numerical and analytical methods. A complete rigorous description of these oscillatory behavior would necessitate multiple scale analysis (with the introduction of fast variable to resolve the oscillatory structure) and an asymptotic matching procedure. However the oscillatory structure has been successfully analyzed only in cases like the KdV equation [25, 24, 45, 46, 47, 34] and the nonlinear Schrodinger equation [38, 39, 71].

The first examples we consider here is the viscous Burgers equation:

$$(4.1) \qquad u_t + u u_x = \nu u_{xx},$$

and the dispersive Burgers equation introduced in [63]:

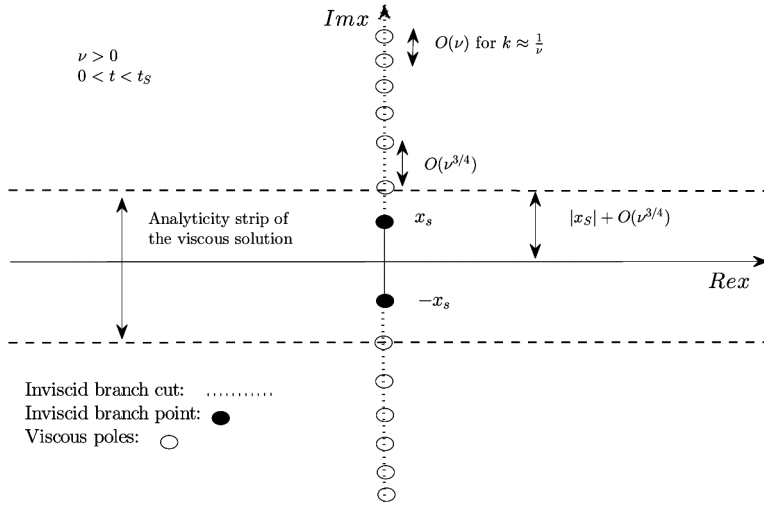$$(4.2) \qquad u_t + u u_x = \epsilon \exp{(i\theta)} u_{xx}.$$

Fig. 8. Inviscid branch points, branch cuts and viscous poles for the viscous Burgers equation (4.1) with $v > 0$ and $0 < t < t_S$.

In [**64, 65, 63**], the authors analyzed the pole dynamics of the above equations. They showed the different behavior of the poles in presence of dissipation versus the presence of dispersion. Their results are summarized in Figs. 8 and 9 and in Fig. 10.
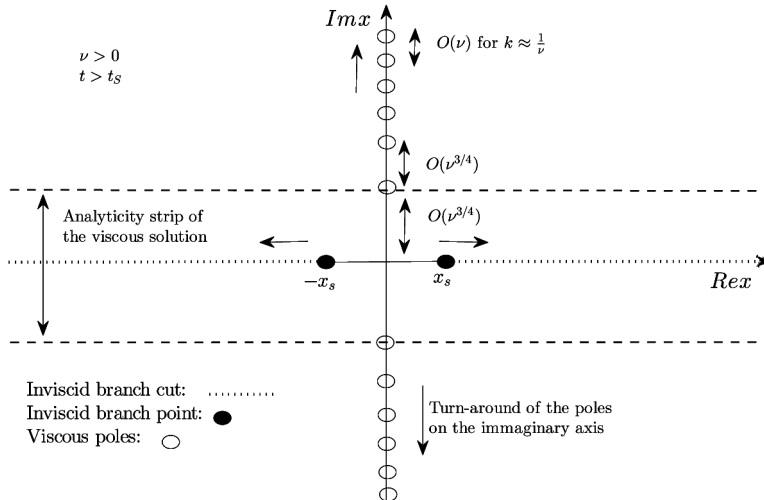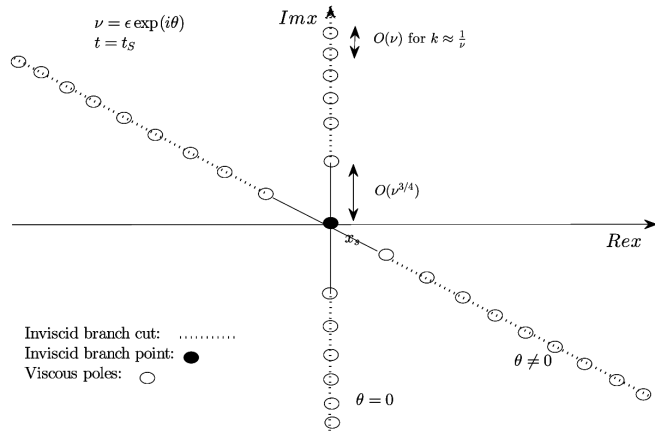

Fig. 9. Inviscid branch points, branch cuts and viscous poles for the viscous Burgers equation (4.1) with $v > 0$ and $t > t_S$.

Fig. 10. Inviscid branch point, branch cuts and viscous poles at the singularity time $t = t_S$ for the dispersive Burgers equation (4.2) with $\nu = \epsilon \exp(i\theta)$.

In the zero-dispersion (or zero-viscosity limit), the complex poles coalesce onto a branch cut, and the zero-dispersion solution is described by branch-cut dynamics. As shown in the previous section, the cube root singularity is known to be a generic
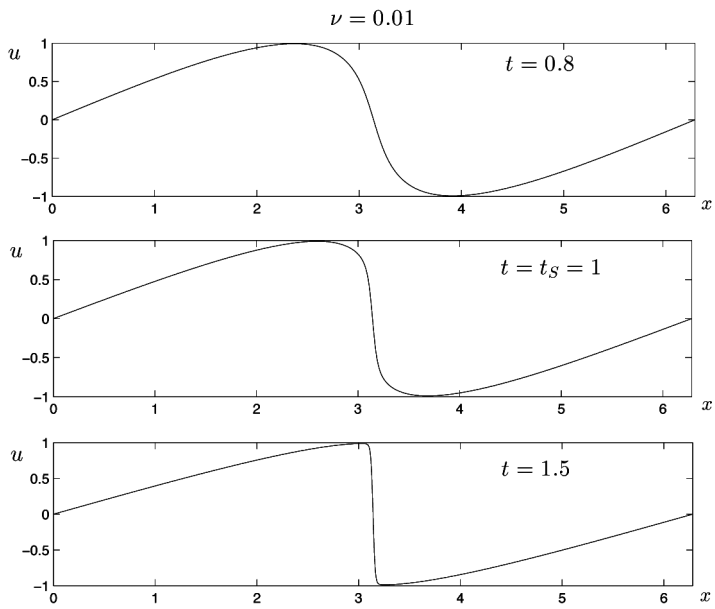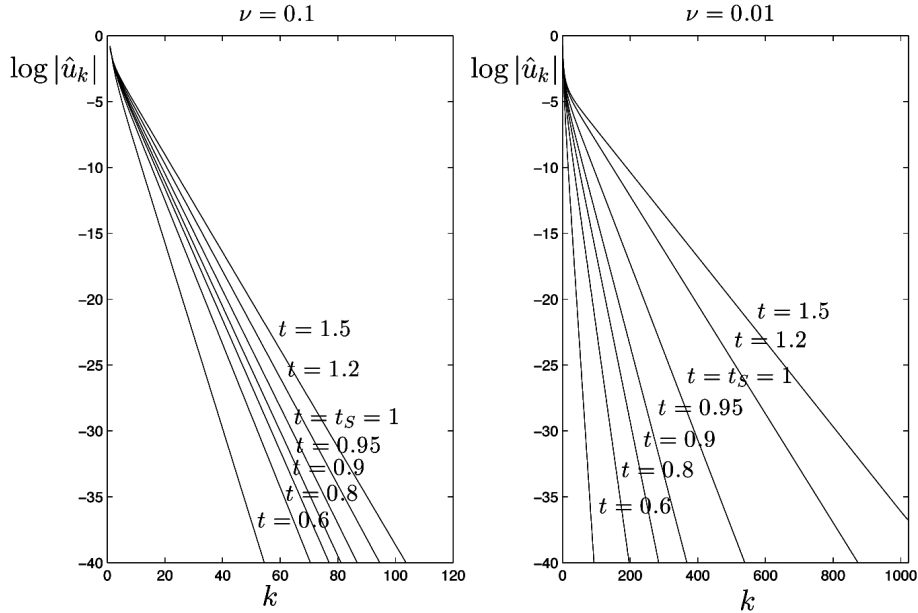

Fig. 11. The evolution in time for the viscous Burgers equation (4.1) with $\nu = 0.01$.

Fig. 12. The spectrum at different times for the viscous Burgers equation (4.1) with $v = 0.01$ and $v = 0.1$.

singularity for the inviscid Burgers equation. It is due to the coalescence of two conjugate branch points of order two in the complex plane [**63**]. In the purely dispersive case, the solution of (4.2) or (4.3) develops rapid oscillations. These oscillations are caused by the presence of complex poles in the solution which have moved close to the real axis. This result is important in providing a tangible cause for the formation of the oscillations.

The above results can be recovered through the application of the techniques presented in the previous Section. To (4.1) and to (4.2) we shall impose the initial datum $u(x, t = 0) = \sin x$.

In Fig. 11 it is shown the evolution in time for the viscous Burgers equation (4.1) with $v = 0.01$ and in Fig. 12 the behavior of its spectrum at different times and different viscosity.

In Fig. 13 it is shown the Padé approximants for the viscous Burgers equation (4.1) with two different viscosity $v = 0.01$ and $v = 0.1$.

In Fig. 14 it is shown the evolution in time for the dispersive Burgers equation (4.2) with $\epsilon = 0.01$ and $\theta = \pi/4$ and in Fig. 15 the behavior of its spectrum at different times and different dispersion value $\epsilon = 0.1$ and $\epsilon = 0.01$.
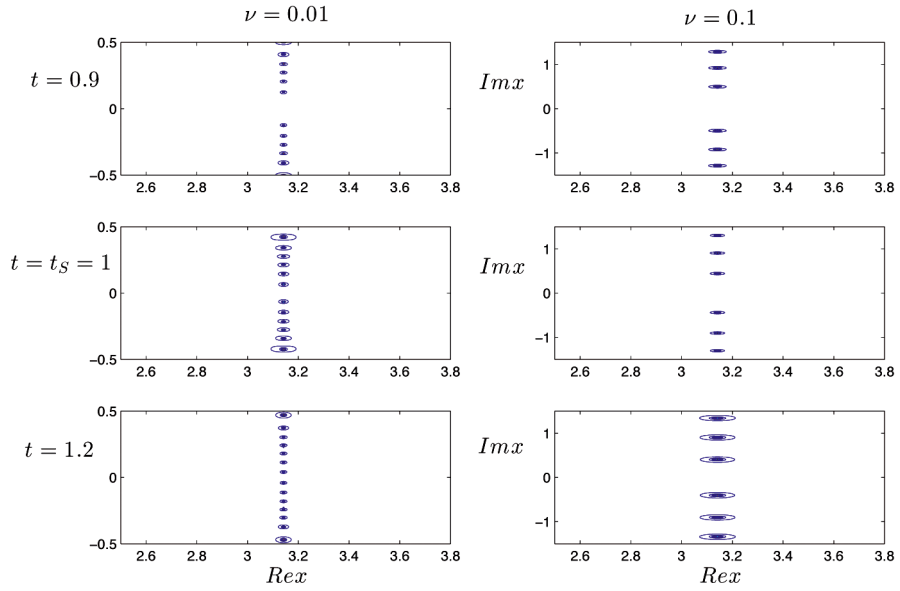
Fig. 13. Viscous poles at different times for the viscous Burgers equation (4.1) with $v = 0.1$ and $v = 0.01$. The Padé analysis results.
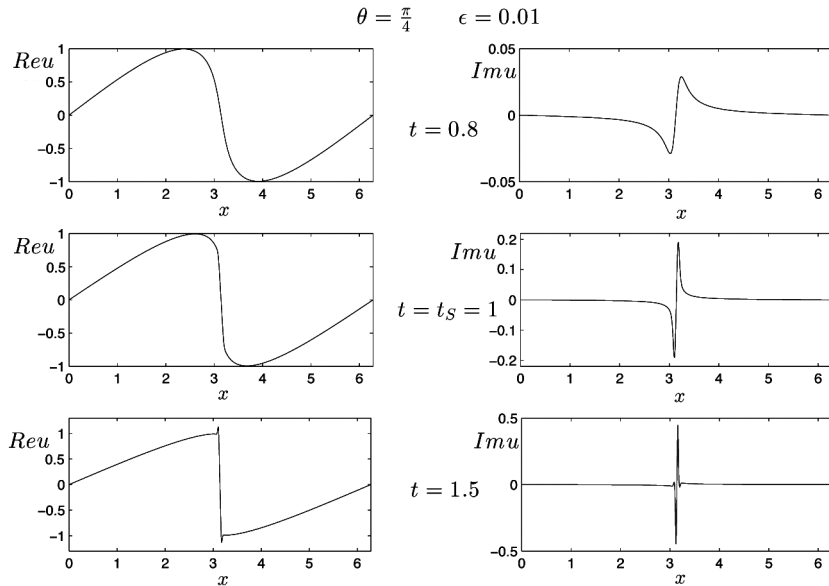

Fig. 14. The evolution in time for the dispersive Burgers equation (4.2) with $\epsilon = 0.01$ and $\theta = \pi/4$.
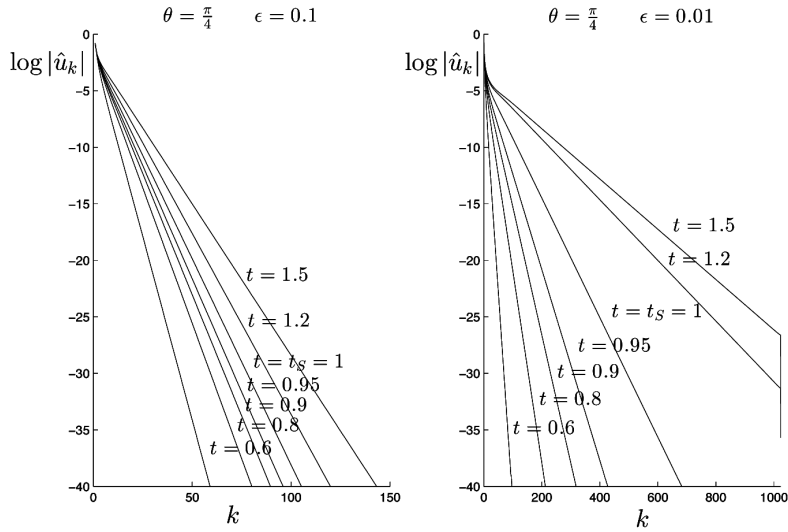
$$\theta = \frac{\pi}{4} \qquad \epsilon = 0.1 \qquad\qquad \theta = \frac{\pi}{4} \qquad \epsilon = 0.01$$

Fig. 15. The spectrum at different times for the dispersive Burgers equation (4.2) with $\epsilon = 0.01$ and $\epsilon = 0.1$ and $\theta = \pi/4$.

In Fig. 16 it is shown the Padé approximants for the dispersive Burgers equation (4.2) with $\epsilon = 0.01$ and $\epsilon = 0.1$, and $\theta = \pi/4$.
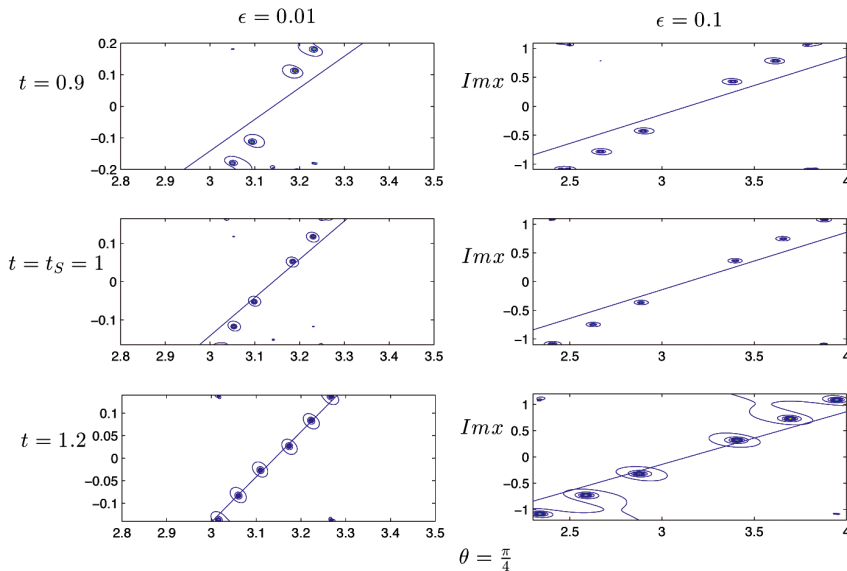
Fig. 16. Complex poles at different times for the dispersive Burgers equation (4.2) with $v = \epsilon \exp(i\theta)$. The Padé analysis results.

One can notice an agreement between the results of [**63**] sketched in Figs. 8, 9 and 10 and our analysis based on the Padé approximants, reported in Fig. 13 for the viscous case and in Fig. 16 for the dispersive cases.

We now pass to the analysis of the KdV equation:

$$(4.3) \qquad u_t + uu_x + \epsilon^2 u_{xxx} = 0$$

which is considered to be the canonical example of dispersive equation. To the above equation we shall impose the initial datum $u(x, t = 0) = \sin x$. We shall see that the solution presents a series of complex singularities. Moreover, in the zero dispersion limit, the singularities approache the real axis and tend to coalesce. The dynamics of the KdV complex singularities seems therefore to be analogous to what we have seen for the dispersive Burgers equation.

In Fig. 17 it is shown the evolution in time for the KdV equation (4.3) with $\epsilon = 0.01$ and in Fig. 18 the behavior of its spectrum at different times and different dispersion value $\epsilon = 0.1$ and $\epsilon = 0.01$.

In Fig. 19 it is shown the Padé approximants for the KdV equation (4.3) with $\epsilon = 0.01$ and $\epsilon = 0.1$.

We perform an analysis of the hidden singularities for the KdV equation applying the BPH and Kida methods. In Figs. 20 and 21 it is shown the indicatrix function
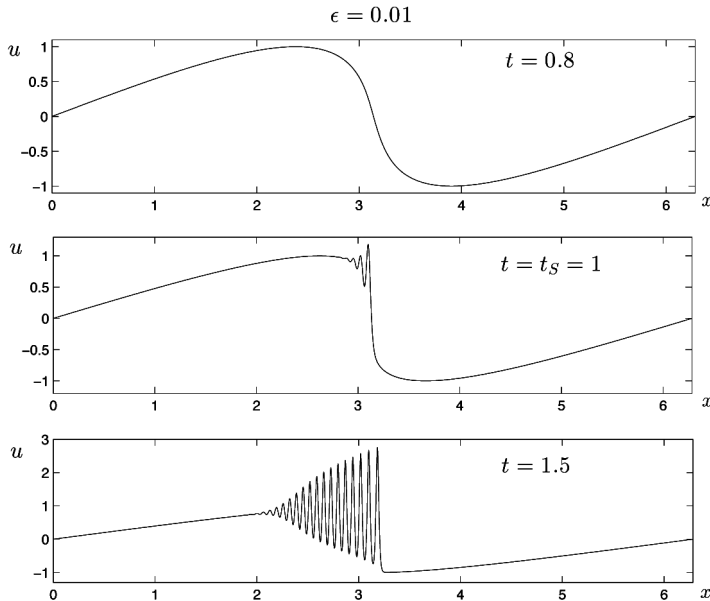

Fig. 17. The evolution in time for the dispersive KdV equation (4.3) with $\epsilon = 0.01$.
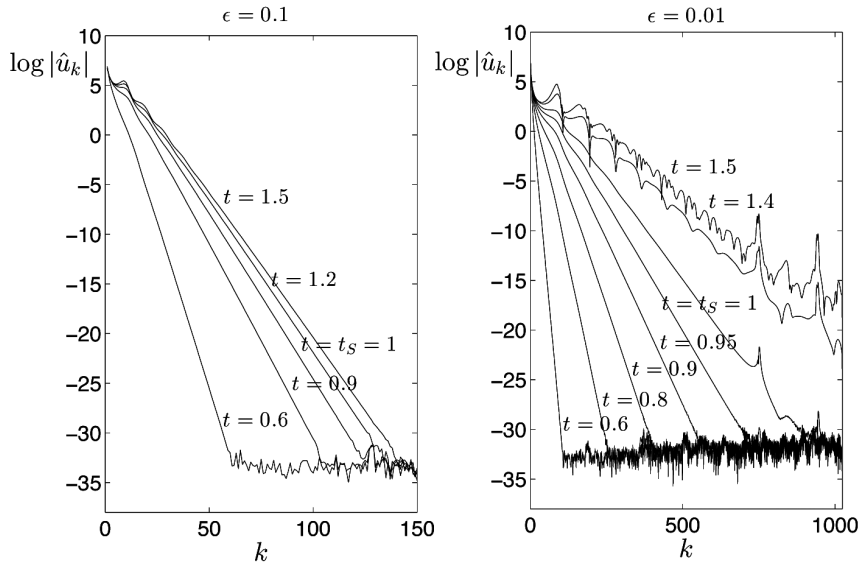
Fig. 18. The spectrum at different times for the dispersive KdV equation (4.3) with $\epsilon = 0.01$ and $\epsilon = 0.1$.
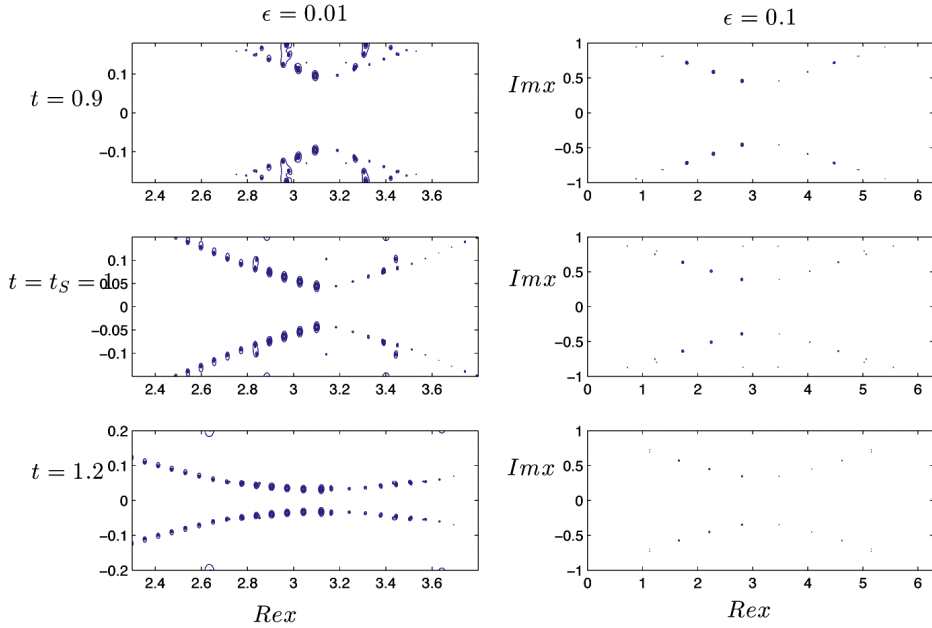

Fig. 19. Poles at different times for the dispersive KdV equation (4.3) with $\epsilon = 0.01$ and $\epsilon = 0.1$. The Padé analysis results.
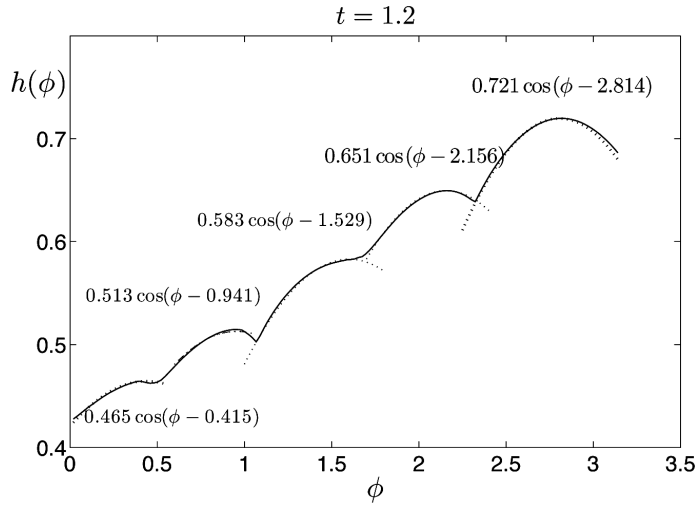
Fig. 20. The indicatrix (3.17) for the dispersive KdV equation (4.3) with $\epsilon = 0.1$ at time 1.2. Dotted lines represent the local fitted cosine functions.

given by (3.17) for the dispersive KdV equation (4.3) with $\epsilon = 0.1$ at time, respectively, $t = 1.2$ and $t = 1.5$. It is also shown the results of the fitting of the piecewise cosine function which gives the location of the singularities. The results are in agreement with the Padé approximant analysis of Fig. 19.
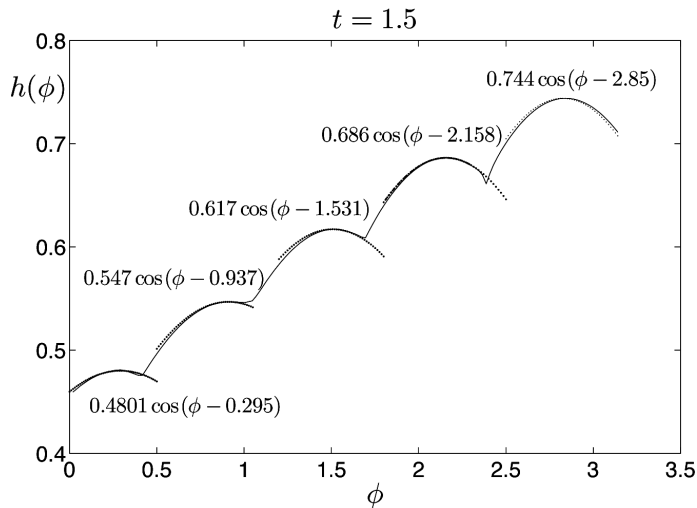

Fig. 21. The indicatrix (3.17) for the dispersive KdV equation (4.3) with $\epsilon = 0.1$ at time 1.5. Dotted lines represent the local fitted cosine functions.
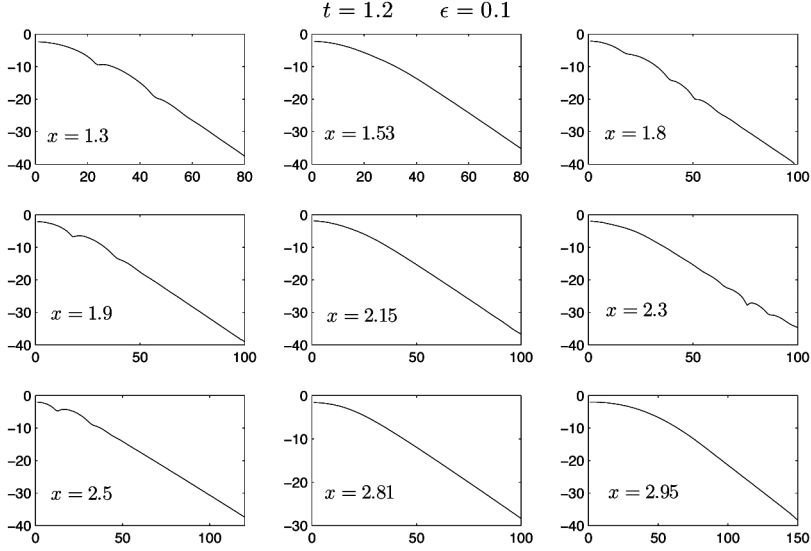
Fig. 22. The Kida filtered spectrum ((3.13) and (3.15)) for the dispersive KdV equation (4.3) with $\epsilon = 0.1$ at time 1.2.

We perform also an analysis using the Kida technique, with $d = 0.2$ in the Gaussian (3.10). In Fig. 22 it is shown the filtered spectrum (3.13) at different locations of x. One can notice that at the singularity locations $x = 1.53$, $x = 2.15$ and $x = 2.81$ the respective filtered spectrum has a linear behavior as predicted by formulas (3.15).

The fitting results at time 1.2 of the Kida filtered spectrum (3.15) for the KdV equation with $\epsilon = 0.1$ at the singularity location $x = 1.53$, $x = 2.15$ and $x = 2.81$ are shown in Table 2. The singularities are complex poles and the respective distances from the real axis are in agreement with the Padé approximant results shown in Fig. 19. The fitting to determine the algebraic characters α of the singularities are performed in the range $1 < k < 5$, while the fitting to calculate the distances δ form the real axis of the singularities are performed in the range $1 < k < 80$.

Table 2. *The fitting results at time* 1.2 *of the Kida filtered spectrum* ((3.13) *and* (3.15)) *for the KdV equation with* $\epsilon = 0.1$ *at the singularity location* $x = 1.53$, $x = 2.15$ *and* $x = 2.81$.

	$x = 1.53$	$x = 2.15$	$x = 2.81$
$\alpha + 1$	0.081	0.098	0.039
δ	0.56	0.45	0.34

4.2 - *Singularity formation for Prandtl equation*

In this section we apply the complex singularity tracking method to investigate the singularity formation for 2D Prandtl equations, and its link with the separation phenomena occurring when an incompressible viscous flow interacts with a rigid boundary.

Prandtl equations are used to describe the boundary layer flow in the zero viscosity limit. These equations are obtained by introducing the following scaling into the Navier-Stokes equations and taking the limit as $Re \to \infty$ (see [62]):

$$(4.4) \qquad y = Re^{-1/2}\,Y, \qquad v = Re^{-1/2}\,V,$$

where y is the normal coordinate, v is the normal component of the velocity, and Y and V are the rescaled coordinate and normal velocity. The equations obtained at first order of the asymptotic expansion are:

$$(4.5) \qquad \frac{\partial u}{\partial t} + u\frac{\partial u}{\partial x} + V\frac{\partial u}{\partial Y} - U_\infty\frac{dU_\infty}{dx} = \frac{\partial^2 u}{\partial Y^2},$$

$$(4.6) \qquad \frac{\partial u}{\partial x} + \frac{\partial V}{\partial Y} = 0,$$

with initial and boundary conditions given by

$$(4.7) \qquad u(x, Y, 0) = U_\infty,$$

$$(4.8) \qquad u(x, 0, t) = V(x, 0, t) = 0, \quad u(x, Y \to \infty, t) = U_\infty,$$

where $U_\infty(x)$ is the inviscid Euler solution at the boundary.

We consider here the classical case of an impulsively started circular cylinder immersed in an uniform background flow. In this case the inviscid Euler solution at the boundary is $U_\infty(x) = 2\sin x$ and the streamwise coordinate x is measured along the cylinder surface from the front stagnation point, and the normal coordinate y is measured from the cylinder surface (see [74]).

The occurrence of a singularity in Prandtl's solution was first proved numerically by van Dommelen & Shen in [74] by using a numerical lagrangian method. For that reason, in the sequel, we call the singularity in Prandtl solution also as the VDS (van Dommelen & Shen) singularity. The work of van Dommelen & Shen was improved by Cowley in [19] where it was investigated the singularity formation for the displacement thickness β_{vDS} and the normal velocity at infinity V_∞ using power time series expansion and approximating them with a special case of Padé approximants. Singularity formation was also analyzed in [29] through the singularity-tracking method applied on the streamwise velocity component u of Prandtl equation, and it was found that for the initial condition $U_\infty(x)/2 = \sin x$, a cubic-root singularity forms at $2t_s \approx 3$ with the blow up of $\partial_x u$ at $(x_s, Y_s) \approx (1.94, 7)$.

The physical effects of the singularity formation in Prandtl solution are shown in Fig. 23 where the evolution of the vorticity up to the singularity time $t_s = 1.5$ for the
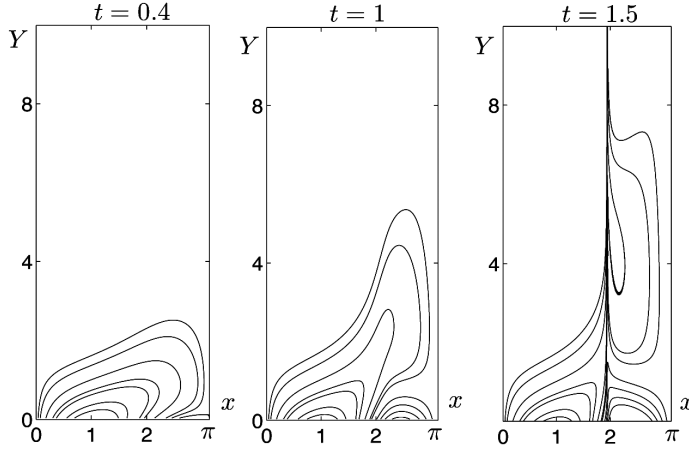
Fig. 23. The evolution of the vorticity of Prandtl's equation for the van Dommelen and Shen initial datum $U_\infty = 2\sin(x)$ at different times. It is visible the formation of a shock at $x \approx 1.94$ at the singularity time $t_s = 1.5$.

VDS initial datum $U_\infty(x) = 2\sin x$ is shown. At time t_s it is visible the singularity at the streamwise location $x \approx 1.94$ where the vorticity is ejected in the outer flow from within the boundary layer (separation).

In this section we investigate the singularity formation for Prandtl wall shear $\tau_w^P = \partial_Y u_{|Y=0}$, in order also to compare the results with the singularity analysis performed on the Navier-Stokes wall shear at different Re numbers (Section 4.3). These results are originally presented in [31].
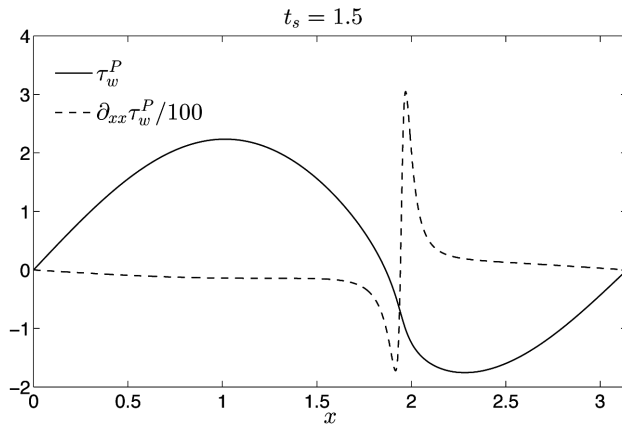

Fig. 24. Prandtl wall shear τ_w^P at the singularity time $t_s = 1.5$ and its rescaled second derivative which shows a singularity at $x_s \approx 1.94$.
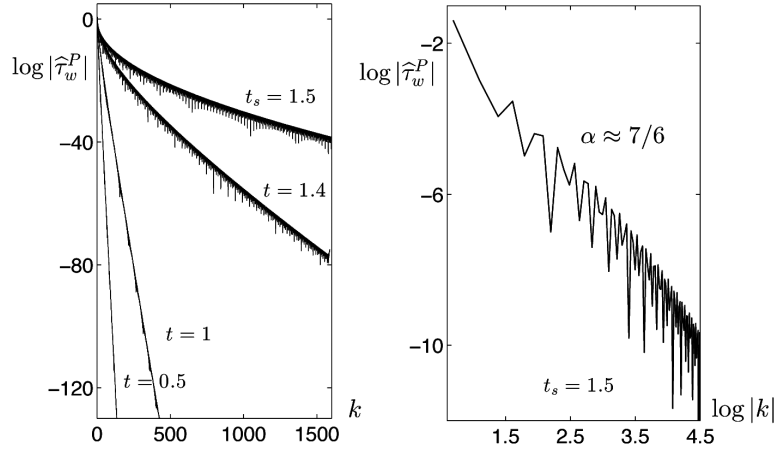
Fig. 25. On the left the Fourier spectrum $\widehat{\tau}_w^P$ of Prandtl's wall shear at various times. On the right, the Fourier spectrum of τ_w^P for Prandtl's wall shear at $t_s = 1.5$ in log-log coordinates: the rate of algebraic decay behaves like $\alpha \approx 7/6$.

In Fig. 24 it is shown Prandtl wall shear at the singularity time $t_s = 1.5$ and its (rescaled) second derivative: a strong eruptive behavior is visible in the second derivative at the streamwise location $x_s \approx 1.94$. In Fig. 25 on the left it is shown the evolution of the spectrum $\widehat{\tau}_w^P$ of the Prandtl wall shear. At the singularity time t_s the spectrum loses the exponential decay and the rate of its algebraic decays at t_s gives the algebraic character of the singularity $\alpha \approx 7/6$, revealing a blow-up in the second derivative of the wall shear as already shown in Fig. 24.
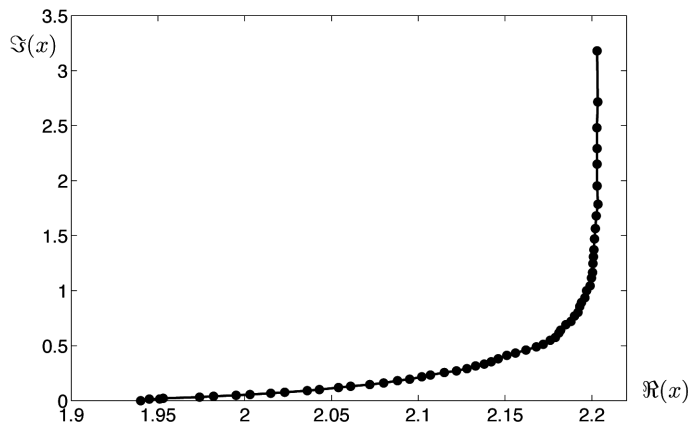

Fig. 26. The time evolution in the complex plane $(\Re(x), \Im(x))$ of the complex singularity of τ_w^P from time 0.1 up to time 1.5. At $t_s = 1.5$, the singularity of τ_w^P hits the real axis at $x_s \approx 1.94$.
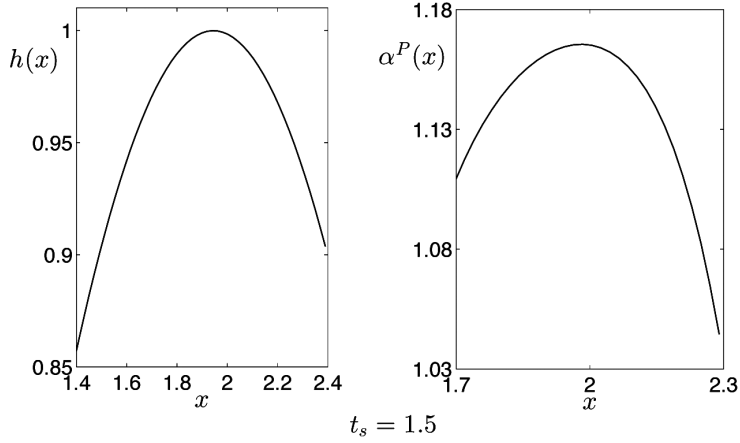
Fig. 27. The indicatrix function $h(x)$ in (3.16) at $t_s = 1.5$ on the left: h behaves like a cosine centered at $x_s \approx 1.94$. On the right, the rate of algebraic decay evaluated from equation (3.16) at $t_s = 1.5$. In $x_s = 1.94$, where the singularity forms, this decay behaves like $\alpha \approx 7/6$.

In Fig. 25 on the right it is shown the Fourier spectrum of τ_w^P at time t_s in log-log coordinates where a slope of $7/6 + 1$ is visible.

We apply the BPH method to Prandtl's wall shear to track the complex singularity in the complex plane, and in Fig. 26 it is shown the time evolution of the singularity of τ_w^P, from $t = 0.1$ to $t_s = 1.5$ with a time step of 0.05. After a transient time in which the singularity is characterized by a movement parallel to the imaginary
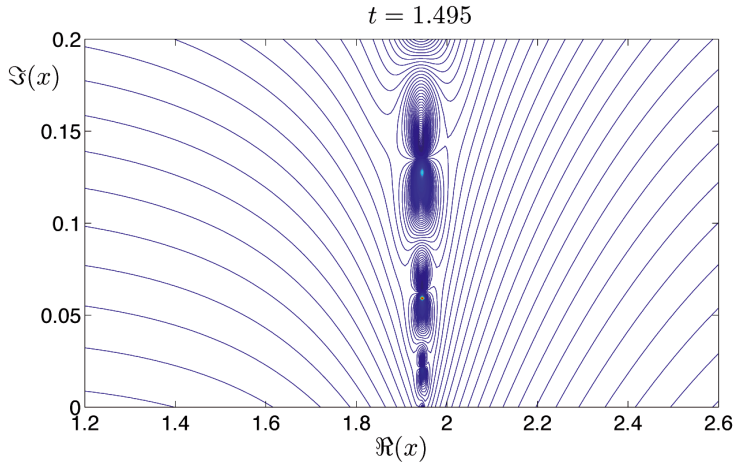

Fig. 28. The contour levels of the modulus of the Padé approximant $P_{250/250}$ of τ_w^P at $t = 1.495$.

axis, the singularity moves toward the position $x_s = 1.94$, hitting the real axis at time $t_s \approx 1.5$. At this time the Fourier spectrum loses exponential decay and the indicatrix function h in (3.16) behaves like a cosine function of amplitude 1 centered in $x_s \approx 1.94$, as it is visible in Fig. 27 on the left. In Fig. 27 on the right, the rate of algebraic decay $\alpha^P(x)$ from (3.16) is shown at $t = t_s$ showing that $\alpha(x = 1.94) \approx 7/6$.

We conclude this analysis evaluating the modulus of the Padé approximant $P_{250/250}$ of τ_w^P at time t close to $t_s = 1.5$. In Fig. 28 one can see the algebraic branch cut, which is visible as a series of poles and zeros along a cut parallel to the imaginary axis and located at $x_s \approx 1.94$.

4.3 - *Singularity analysis for Navier Stokes solutions*

In [**54, 55, 30, 31**] it was shown that the wall shear τ_w^{NS} of Navier-Stokes solution is a relevant indicator of the onset of the various viscous-inviscid interactions characterizing the separation process in Navier-Stokes solutions. In fact, after the formation of the back-flow, the first relevant interaction visible in Navier-Stokes solutions, i.e. the so called large-scale interaction, leads to the disagreement between the Navier-Stokes and Prandtl wall shear. The subsequent small-scale interaction, observable only for moderate-high Re numbers, characterizes the typical turbulent chaotic regime of the high Re number flow with high gradients formation in τ_w^{NS}. In [**31**] it was found a relationship between these interactions and the presence of complex singularities in τ_w^{NS}. We present in this section the results due to the singularity analysis of the wall shear τ_w^{NS} for the impulsively started disk case, allowing also a direct comparison with the Prandtl case.

The Navier-Stokes equations in the vorticity-streamfunction formulation for the impulsively started disk read as:

$$(4.9) \qquad \frac{\partial \omega}{\partial t} + \frac{u}{r}\frac{\partial \omega}{\partial \theta} + v\frac{\partial \omega}{\partial r} = \frac{1}{Re}\left(\frac{1}{r^2}\frac{\partial^2 \omega}{\partial \theta^2} + \frac{1}{r}\frac{\partial \omega}{\partial r} + \frac{\partial^2 \omega}{\partial r^2}\right),$$

$$(4.10) \qquad \frac{1}{r^2}\frac{\partial^2 \psi}{\partial \theta^2} + \frac{1}{r}\frac{\partial \psi}{\partial r} + \frac{\partial^2 \psi}{\partial r^2} = -\omega,$$

$$(4.11) \qquad u = \frac{\partial \psi}{\partial r}, \quad v = -\frac{1}{r}\frac{\partial \psi}{\partial \theta},$$

$$(4.12) \qquad u = v = 0, \qquad r = 1,$$

$$(4.13) \qquad \omega \to 0, \qquad r \to \infty,$$

$$(4.14) \qquad \omega(\theta, r, t = 0) = 0,$$

$$(4.15) \qquad \psi(\theta, r, t = 0) = \left(r - \frac{1}{r}\right)\sin\theta.$$

Equation (4.9) is the vorticity-transport equation, equation (4.10) is the Poisson equation for the streamfunction, and equations (4.11) relate the velocity components to the streamfunction. (4.12) and (4.13) are the no-slip and impermeability conditions on the circular cylinder and the irrotational condition at infinity, respectively. The initial condition (4.14) expresses the irrotationality condition of the flow at the initial time, (4.15) is the initial condition for the streamfunction. The walls shear is as usually defined as $\tau_w^{NS} = -\omega_{r=1}/\sqrt{Re}$. The problem is solved in the domain $[0, \pi] \times [1, \infty)$, and only the upper part of the circular cylinder is considered owing to symmetry. Details on the numerical scheme used can be found in [**31**].

In [**31**] it was shown that τ_w^{NS} has several singularities that can be divided into three distinct groups. These three groups of singularities are visible in Fig. 29 in which it is shown the modulus of the Padé approximant $P_{300/3000}$ of τ_w^{NS} for $Re = 10^5$ at $t = 1.58$: at this time the large and small scale interactions have already formed for $Re = 10^5$. The left group comprehends only a singularity. The middle group comprehends several complex singularities corresponding to the large-scale interaction. The right group is visible only for moderate-high Re number, and consists of complex singularities that correspond to the small-scale interaction.
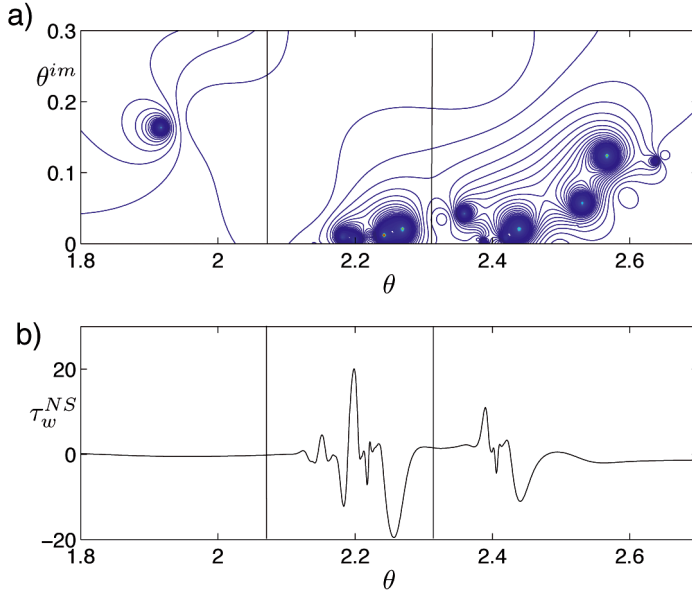

Fig. 29. **a)** The contour levels of the modulus of the Padé approximant $P_{300/300}$ of τ_w^{NS} for $Re = 10^5$ at $t = 1.58$. Three distinct groups of complex singularities are present. Each group correspond to a different viscous-inviscid interaction. **b)** The wall shear τ_w^{NS}: a strong correspondence between the high gradients in τ_w^{NS} and the positions of the complex singularities in **a)** is visible.
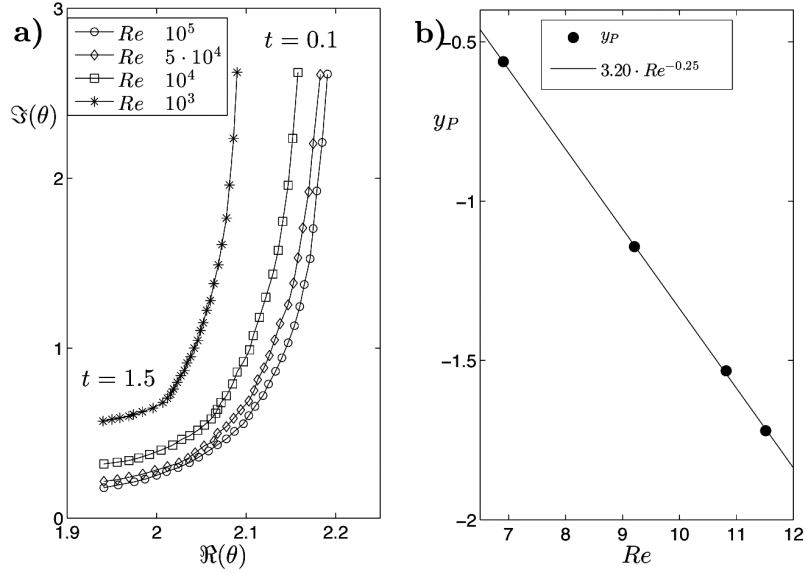
Fig. 30. **a)** The time evolutions in the complex plane $(\Re(\theta), \Im(\theta))$ of the complex singularities s_P of τ_w^{NS} for the various Reynolds numbers from time 0.1 up to time 1.5 with time step of 0.05. At $t_s = 1.5$ the singularity remains at a distance y_P from the real axis which goes like $3.2 \cdot Re^{-0.25}$. **b)** The distance y_P is shown versus the Reynolds numbers in log-log coordinates.

The first singularity of τ_w^{NS} in the left group as shown in Fig. 29a is comparable with the singularity of Prandtl wall shear τ_w^P (hereafter we shall denote this singularity as s_P). The main similarity between s_P and the singularity of τ_w^P lies in their
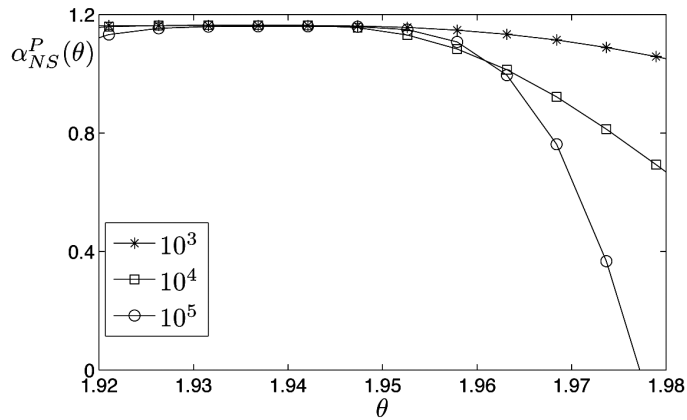

Fig. 31. The characterization α_{NS}^P of the complex singularity s_P of τ_w^{NS} evaluated through the BPH method. At $t_s = 1.5$ in $\theta \approx 1.94$ we retrieve $\alpha_{NS}^P \approx 7/6$ for all the Re considered.

characterization. In fact, through the BPH method we have obtained that the algebraic characterization of s_P at the time $t_s = 1.5$ is $\alpha_{NS}^P \approx 7/6$ for each Reynolds number (see Fig. 31) which is the same characterization observed for τ_w^P as shown in the previous section. We stress that as compared to the Prandtl case, the characterization of α_{NS}^P has been more difficult to evaluate. This was mainly due to the presence of the various complex singularities of the other groups that affect the indicatrix function leading to some difficulties in handling numerically the evaluation of the algebraic decay rate. The second similarity between s_P and the singularity of τ_w^P is given by the similar time evolution of their positions in the complex plane as shown in Figure 30a (singularities are tracked from $t = 0.1$ to $t_s = 1.5$ with time step
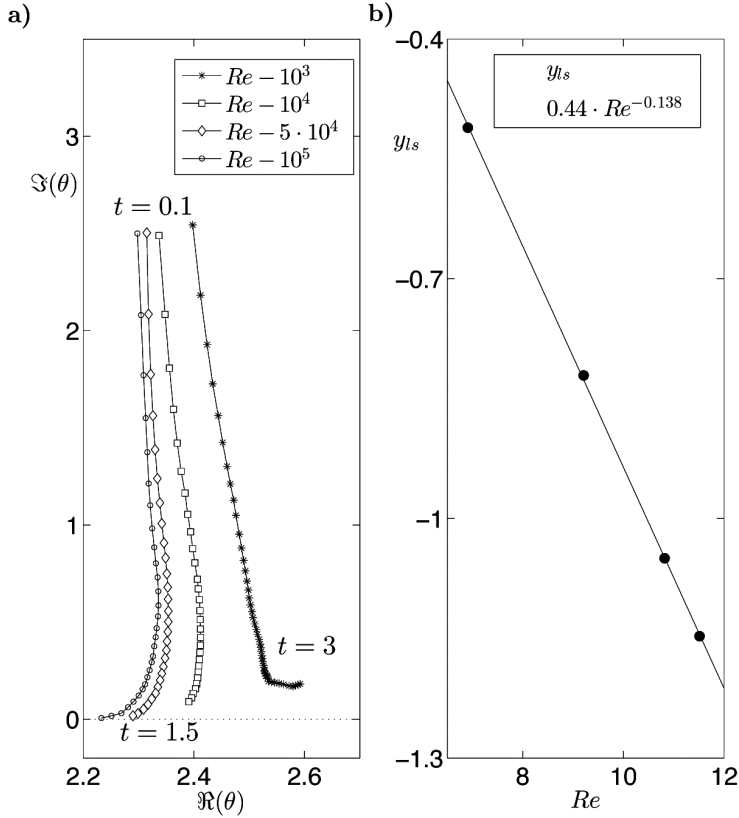

Fig. 32. **a)** The time evolution in the complex plane $(\Re(\theta), \Im(\theta))$ of the complex singularity s_{ls} of τ_w^{NS} for $Re = 10^3$ from time 0.1 up to time 3 with time step of 0.05, and for $Re = 10^4, 5 \cdot 10^4, 10^5$ from time 0.1 up to time 1.5 with time step of 0.05. **b)** The distance y_{ls} of s_{ls} from the real domain versus the Reynolds number in log-log coordinates at the time at which large-scale interaction begins. The singularity is at a distance y_{ls} from the real axis that goes like $0.44 \cdot Re^{-0.138}$.
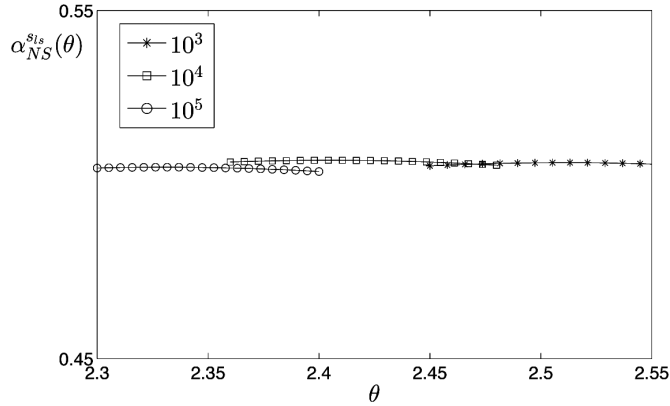
Fig. 33. The characterization $\alpha_{NS}^{s_{ls}}$ of the complex singularity s_{ls} of τ_w^{NS} evaluated from the BPH method. At $t = 1.05$, $\alpha_{NS}^{s_{ls}} \approx 0.5$ for $Re = 10^3, 10^4, 10^5$, and s_{ls} is located at $(2.501, 0.54), (2.40, 0.37), (2.32, 0.28)$, respectively.

of 0.05, see also Fig. 26 for the time evolution of the Prandtl wall shear in the complex plane). All singularities rapidly move toward the real axis slightly shifting upstream on the circular cylinder. At time $t_s = 1.5$, when singularity forms in Prandtl solution, all the singularities have the real part of their position close to $x_s \approx 1.94$, and the imaginary part y_P which follows the rule $y_P = C_P Re^{\lambda_P}$, where $\lambda_P \approx -0.25$ and $C_P \approx 3.2$ (see in Figure 30b, where y_P is shown versus the Reynolds number in log-log scale). While it is clearly expected that s_P get closer to the real domain ad Re increases, it was less predictable, mainly due to the influences of the other singularities, that s_P moves toward the position $x_s = 1.94$ for all the Re.

The second group of complex singularities in τ_w^{NS} is related to the large-scale interaction developing in the separation process, and it exists for all the Reynolds number considered. The presence of several singularities close to each other leads to numerical difficulties in resolving all the singularity positions and characterizations. Only the singularity closest to the real axis for all time (hereafter we shall call this singularity s_{ls}) can be well resolved. Also for s_{ls} we have tracked in time the position in the complex plane for all the Re (see Fig. 32). While the evolution of s_{ls} is quite similar for all $Re > 10^3$, a different behavior is observed for $Re = 10^3$. In this case, in fact, s_{ls} continues to shift downstream along the circular cylinder even after total detachment of the boundary layer. For the other Re cases, instead, s_{ls} changes its motion by shifting upstream along the circular cylinder during the small-scale interaction phase. At the time in which large scale interaction begins (from the analysis performed in [31] this interaction forms at $t \approx 0.908, 0.916, 0.94, 0.952$ for $Re = 10^3, 10^4, 5 \cdot 10^4, 10^5$) the distance y_{ls} from the real axis of the singularity s_{ls} follows the rule $y_{ls} = C_{ls} Re^{\lambda_{ls}}$, where

$\lambda_{ls} \approx -0.138$ and $C_{ls} \approx 0.447$, as one can see in Figure 32b, where y_{ls} is shown versus the Re number in log-log coordinates. By applying the BPH method, we have well resolved the characterization of the singularity s_{ls} in the range of time between $t = 0.95$ and $t = 1.1$ when the other complex singularities are still far enough away from the singularity s_{ls}. The charachterization is $\alpha_{NS}^{s_{ls}} \approx 0.5$ for all the Reynolds numbers considered as shown in Fig. 33, where the rate of algebraic decay $\alpha_{NS}^{s_{ls}}$, obtained from equation (3.16), is shown at $t = 1.05$ for the various Reynolds numbers.

The third group of singularities are related to the small-scale interaction, and as for the second group of singularities we were able to well resolve only the primary singularity of this group that is always closest to the real axis (hereafter this singularity is called s_{ss}). In Fig. 34a the time evolution of the position of s_{ss} in the
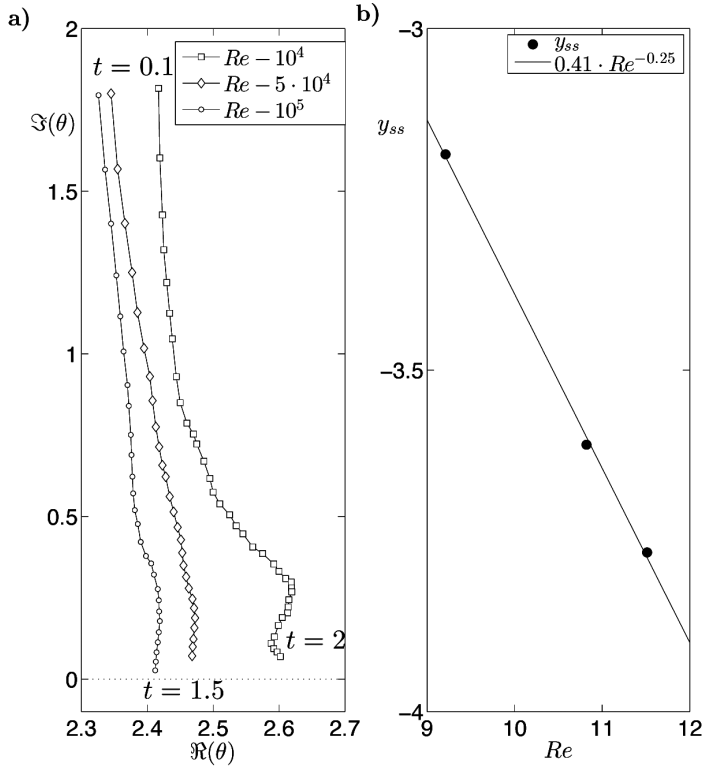

Fig. 34. **a)** The time evolution in the complex plane $(\Re(\theta), \Im(\theta))$ of the complex singularity s_{ss} of τ_w^{NS} for $Re = 10^4$ from time 0.1 up to time 2 with time step of 0.05 and for $Re = 5 \cdot 10^4, 10^5$ from time 0.1 up to time 1.5 with time step of 0.05. **b)** The distance y_{ss} of s_{ss} from the real domain is shown versus the Reynolds number in log-log coordinates at the time in which the small-scale interaction begins. The singularity is at a distance from the real axis that goes like $0.41 \cdot Re^{-0.25}$.

complex plane for $Re = 10^4$ from time $t = 0.1$ up to time $t = 2$, and for $Re = 5 \cdot 10^4$ and $Re = 10^5$ for $t = 0.1$ up to $t = 1.5$ with time step of 0.05. This evolution is not as smooth as compared to that of s_P and s_{ls}, and in [31] the physical events affecting the time evolution of s_{ss} were explained. At the time at which small-scale interaction begins (from the analysis performed in [31] this interaction forms at $t \approx 1.505, 1.29, 1.26$ for $Re = 10^4, 5 \cdot 10^4, 10^5$), it has been observed that the distance y_{ss} from the real axis of the singularity s_{ss} follows the rule $y_{ss} = C_{ss} Re^{\lambda_{ss}}$, where $\lambda_{ss} \approx -0.25$ and $C_{ss} \approx 0.41$. This can be seen in Fig.34b, where y_{ss} is shown versus the Reynolds number in log-log coordinates. The characterization of s_{ss} was quite well resolved at the time in which small scale interaction begins, and we have obtained the value $\alpha_{NS}^{ss} \approx 0.5$. This characterization is compatible with the kind of gradient that forms in τ_w^{NS} as it clearly shows a growth in the first derivative.

5 - Complex singularity tracking method for multivariable function

In this section the singularity-tracking method is extended to a bi-variate function (see [50, 58] for details).

Given a periodic function that can be expressed as a Fourier series

$$u(x_1, x_2) = \sum_{k_1, k_2} u_{k_1 k_2} e^{ik_1 x_1} e^{ik_2 x_2},$$

if one considers those modes (k_1, k_2) such that $k_1 = k \cos \theta$ and $k_2 = k \sin \theta$, where $k = |(k_1, k_2)|$, then the asymptotic behavior of the Fourier coefficients in the Fourier **k**-space with $k \to \infty$ have the following asymptotic behavior:

(5.1) $u_{k_1 k_2} \approx k^{-(\alpha(\theta)+1)} e^{-\delta(\theta)k} e^{ikx^*(\theta)}$ where $(k_1, k_2) = k(\cos \theta, \sin \theta)$.

The width of the analyticity strip δ^* is the minimum over all directions θ, i.e. $\delta^* = \min_\theta \delta(\theta)$.

A second way to extend the singularity tracking method to bi-variate functions is to define the shell-summed Fourier amplitudes, are defined as

(5.2) $$A_K \equiv \sum_{K \leq |(k_1, k_2)| < K+1} |u_{k_1 k_2}|,$$

which are a kind of discrete angle average of the Fourier coefficients. The asymptotic behavior of these amplitudes is

(5.3) $$A_K \approx C K^{-(\alpha_{Sh}+1/2)} \exp(-\delta_{Sh} K)   \text{when}   K \to \infty,$$

where δ_{Sh} gives the width of the analyticity strip, while the algebraic prefactor α_{Sh}

gives information on the nature of the singularity. As pointed out in [**58**], using a steepest descent argument, one can see that the two techniques are equivalent. In fact, if one denotes with θ^* the angle where $\delta(\theta)$ takes its minimum (i.e. $\delta^* = \delta(\theta^*)$), one has that $\delta_{Sh} = \delta(\theta^*)$ and that $\alpha_{Sh} = \alpha(\theta^*) - 1/2$.

An interesting situation is when the most singular direction coincides with one of the coordinate axes, e.g. $\theta^* = 0$ (similar is the case when $\theta^* = \pi/2$), which means that (see (5.1)):

$$(5.4) \qquad u_{k_1 0} \approx k_1^{-(\alpha(\theta^*)+1)} e^{-\delta(\theta^*)k_1} \qquad \text{with} \quad \theta^* = 0 \; .$$

In this case it is easy to see that, to evaluate the width of the strip of analyticity, one can consider the variable x_2 as a parameter (when $\theta^* = \pi/2$ one can be consider instead x_1 as a parameter) and adopt the following procedure. First take the Fourier expansion relative to the variable x_1:

$$u(x_1, x_2) = \sum_{k_1} u_{k_1}(x_2) e^{-ik_1 x_1} \; ;$$

second, given that for fixed x_2 the function $u(x_1, x_2)$ is analytic in x_1, use that the spectrum has the asymptotic behavior:

$$(5.5) \qquad u_{k_1}(x_2) \approx k_1^{-(\alpha(x_2)+1)} e^{-\tilde\delta(x_2)k_1} \; ;$$

third use the definition of $u_{k_1 0}$ to write:

$$(5.6) \quad u_{k_1 0} = \int u_{k_1}(x_2) e^{ik_2 x_2} \, dx_2 \approx \int k_1^{-(\alpha(x_2)+1)} e^{-\tilde\delta(x_2)k_1} e^{ik_2 x_2} \, dx_2 \approx e^{-\min_{x_2} \tilde\delta(x_2)k_1} \; ,$$

where, to get the last estimate, we have used a steepest descent argument. Comparing (5.4) with (5.6) one finally derives that, when $\theta^* = 0$:

$$\delta(\theta^*) = \min_{x_2} \tilde\delta(x_2) \; .$$

The procedures needed to capture the asymptotic behavior of the spectrum require high numerical precision and in fact, in the calculations we shall present, we have used a 32–digits precision (using the ARPREC package). For more details on the method and on the various techniques introduced in the literature to fit the spectrum, see [**11, 27, 33, 50, 57, 66, 69**].

5.1 - *Prandtl equation*

We apply the techniques of singularity tracking method for multivariable function, explained in the previous section, to analyze the singularity of the Prandtl solution for the VDS initial datum $U_\infty = 2\sin(x)$ (see Section 4.2).
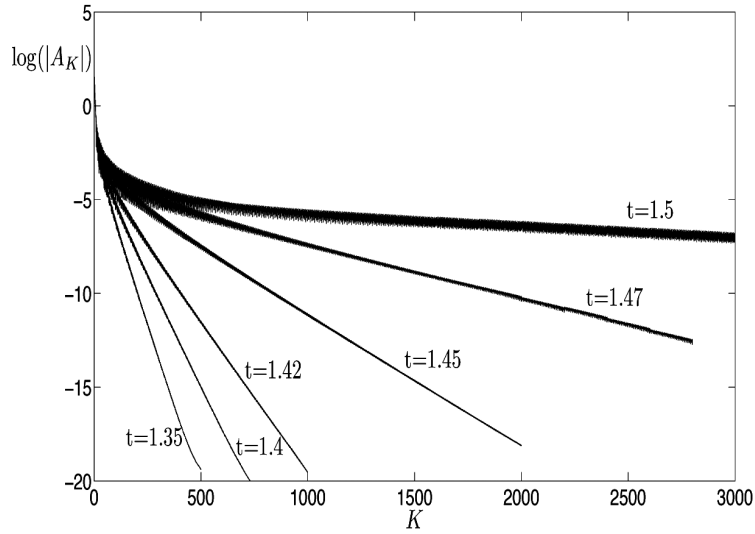
Fig. 35. The behavior in time of the shell summed Fourier amplitude up to the singularity time.

In Fig. 35 we show the shell-summed Fourier amplitudes, where it is evident the loss in time of the exponential decay. Fitting these data using formula (5.3), we get the evolution in time of the width of the analyticity strip, shown in Fig. 36(b), and the
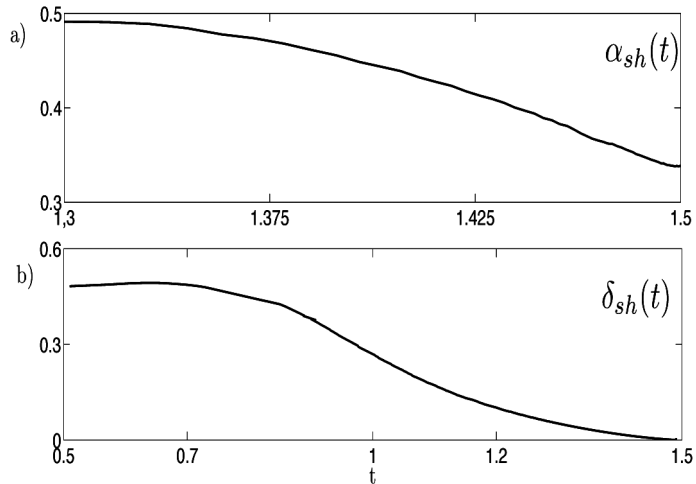

Fig. 36. **a)** The behavior of the algebraic character of the singularity from the shell summed Fourier amplitude of Prandtl's solution. The singularity is of cubic-root type. **b)** The behavior in time of the width of the analyticity strip. The singularity time is $t_s \approx 1.5$.
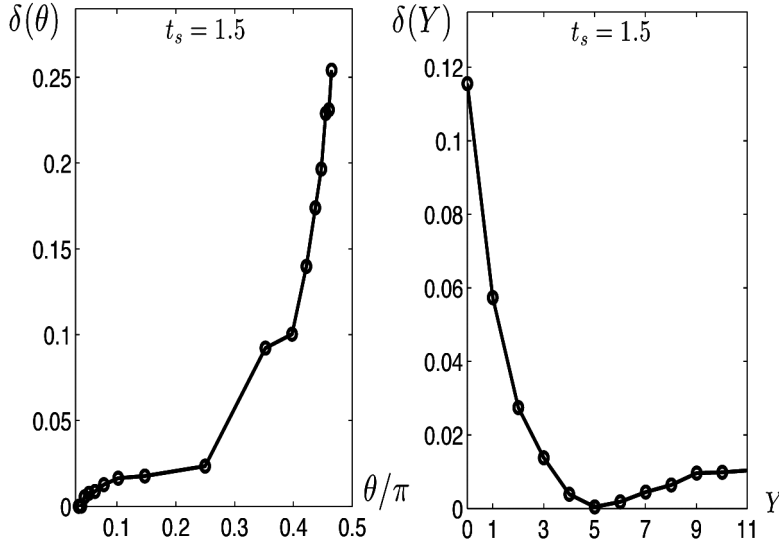
Fig. 37. On the left the fitting of the exponential decay δ at different directions θ of the bi-dimensional Fourier spectrum of Prandtl's solution at the singularity time t_s. The most singular direction is at $\theta = 0$. On the right, the estimates of the exponential decay δ of the Fourier spectrum of Prandtl's solution at time t_s, in terms of the normal variable Y. The location of the minimum, $Y \approx 5$, is the location of the singularity.

algebraic characterization of the singularity in Fig. 36(a). At the critical time $t_s = 1.5$, the solution loses analyticity as a cubic-root singularity. Analyzing the Fourier spectrum of Prandtl solution u at the singularity time t_s using formula (5.1), in Fig. 37 on the right we show the angular dependence of δ where it is visible that the most singular direction is at $\theta = 0$. As explained in the previous section, this result allows to treat the normal variable Y as a parameter, and on the right of the same Figure we show the dependence of δ on Y at the singularity time t_s using formula (5.5). Because $\delta(Y)$ attains its minimum at $Y \approx 5$, this implies that the singularity is located at $Y \approx 5$ and we apply the singularity tracking method to the one dimensional function $u(x, 5)$, whose evolution in time is shown in Fig. 40 where the shock at $x^\star \approx 1.94$ is visible at time t_s.

In Fig. 39 it is shown the behavior in time of the Fourier spectrum at the location $Y = 5$ of u and in Fig. 38 one can see the results of the singularity tracking method at the location $Y = 5$, showing again the formation of a cubic root singularity at time $t_s = 1.5$. What is important now is the determination of the real tangential location of the singularity x^*, which is founded with a study of the oscillatory behavior of the spectrum depurated by the exponential and algebraic decay, using formula (2.1).
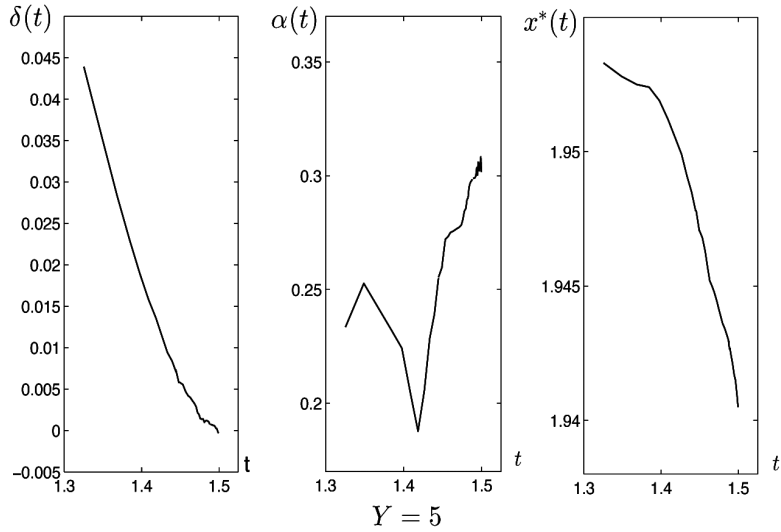
Fig. 38. The results of the singularity tracking for the spectrum of the solution of Prandtl's equation at the location $Y = 5$.
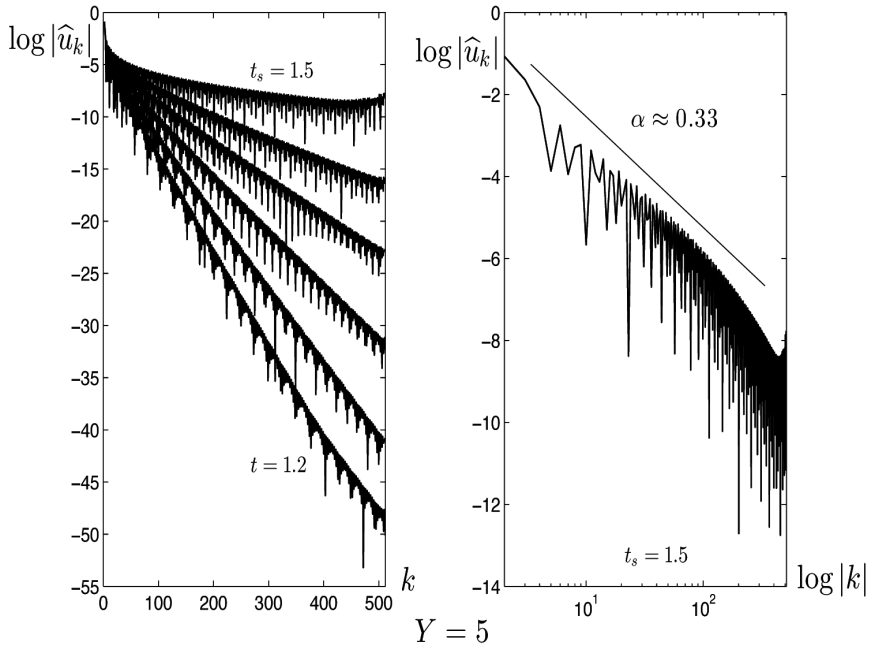
Fig. 39. On the left the spectrum of the solution of Prandtl's equation at the location $Y = 5$ from time $t = 1.2$ up to the singularity time $t_s = 1.5$ with increments of 0.05. On the right the Fourier spectrum of Prandtl's solution at the singularity time t_s and $Y = 5$ in log-log coordinates. It is visible the lose of the exponential decay while the rate of the algebraic decay is $\alpha \approx 0.33$.
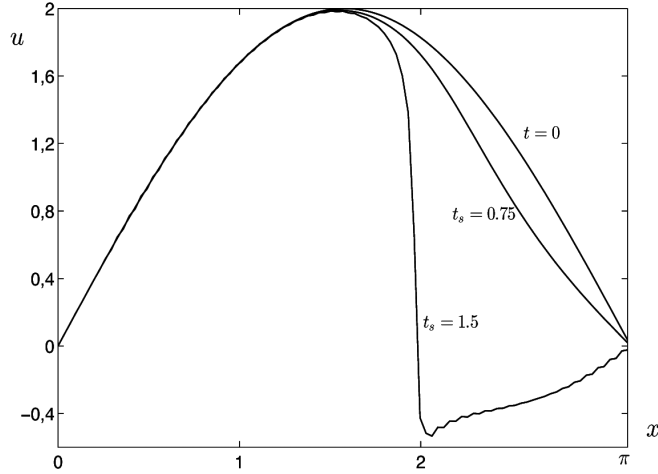
Fig. 40. The solution of Prandtl's equation at the location $Y = 5$ for van Dommelen and Shen initial datum $U_\infty = 2\sin(x)$ at different times. It is visible the formation of a shock at $x \approx 1.94$ at the singularity time $t_s = 1.5$.

This complete the analysis of the singularity of Prandtl's solution in the case of an impulsively started disk. The details of these results are in [**29, 21, 28**].

5.2 - *Navier-Stokes equation*

In this section we present the results obtained by applying the singularity ana-lysis for the 2D spectrum of the velocity component $u(r, \theta)$ of the Navier-Stokes solutions obtained from (4.11) for different Reynolds number (see [**31**] for more details). To perform this analysis we have mapped the physical domain of the various solutions to $\Lambda = [1, 2]$ so that the points in Λ are the Gauss-Lobatto points $\kappa_i = \cos(i\pi/N)_{i=0,\dots,M}$ in Λ. By introducing the points $\zeta_i = \arccos \kappa_i$ we can write Navier-Stokes solution as

$$(5.7) \qquad u(\theta, \zeta, t) \approx \sum_{k=-K/2}^{k=K/2} \sum_{j=0}^{j=M} u_{kj}(t) e^{ik\theta} \cos(j\zeta),$$

and the singularity-tracking method is applied on the Fourier coefficients u_{kj}.

The time evolution of the rate of exponential decay δ_{NS} in (5.3) in shown in Fig. 41a for various Reynolds numbers. The various time evolutions are similar in all cases, and after the formation of a maximum value δ_{NS}^M in time, δ_{NS} decreases as the gradients in the θ direction become intense. For all the Reynolds numbers con-sidered, δ_{NS} has a local minimum δ_{NS}^m in time after $t_s = 1.5$, and after this event it
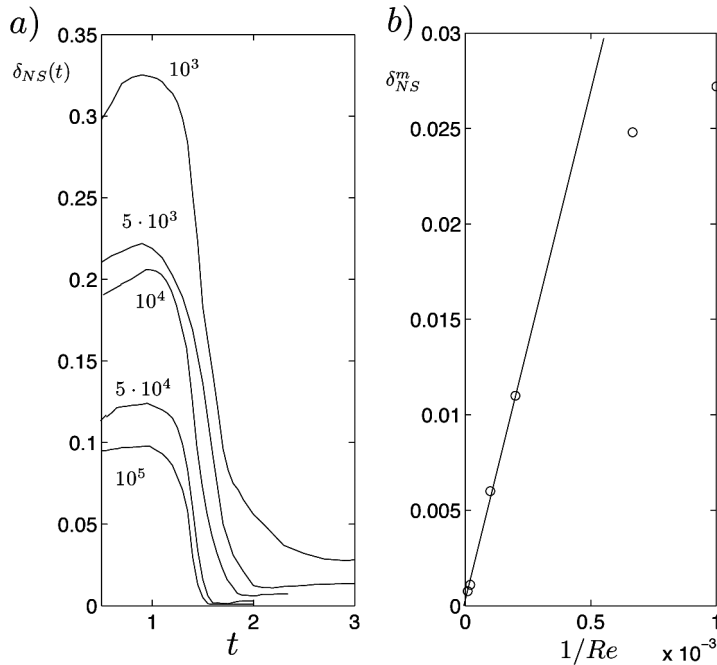
Fig. 41. **a)** Time evolution of δ_{NS} for various Reynolds numbers. δ_{NS}^m has a minimum in time which is of order $O(1/Re)$ as shown in **b)** (at least for the Reynolds numbers for which small-scale interaction forms).

then begins to increase again. It is worth noting that the minimum in time δ_{NS}^m seems to scale linearly with respect to $1/Re$ for the Reynolds numbers for which small-scale interaction occurs (see also Fig. 41b). Regarding the evaluation of α_{NS} we first observe that all of the spectra analyzed have several structures leading to several difficulties in determining the correct value of this charachterization. At the onset of large-scale interaction, when the spectrum is more easily handled, a fitting of the Fourier amplitudes always gives results in the range $0.45 < \alpha_{NS} < 0.55$ for all of the Reynolds numbers considered, suggesting that the value $\alpha_{NS} = 1/2$ is the more probable characterization. For instance, in Fig. 42 the behavior of the Fourier amplitudes A_K for $Re = 10^5$, is shown in log-log coordinates: the linear behavior of the first range of Fourier amplitudes, whose slope returns the rate of algebraic decay, compares with the straight line of slope -1, and this supports the prediction that $\alpha_{NS} = 1/2$.

A relevant feature of the small-scale interaction is the formation of a bulge in the 2D spectra of the solutions for the Reynolds numbers for which this interaction
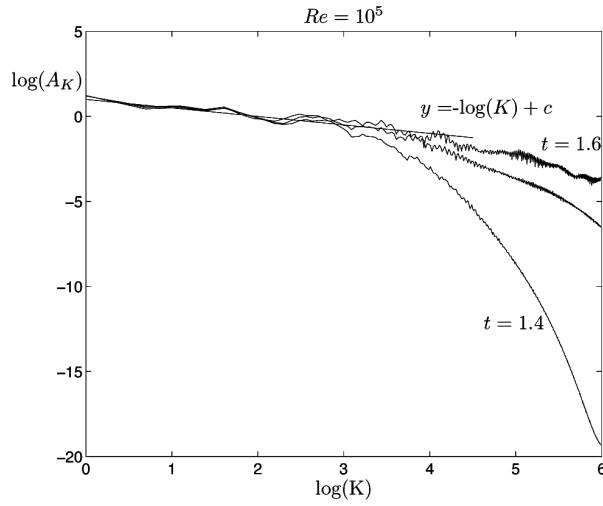
Fig. 42. The behavior for different times (in increments of 0.1) of the shell-summed Fourier amplitudes A_K for $Re = 10^5$ in log-log coordinates. The first linear range of the amplitudes seems to have a slope equal to -1.

forms. In Figs. 43-44 the spectra are shown at different times for $Re = 1.5 \cdot 10^3$ and 10^5 with the most singular direction indicated by a straight line. For $Re = 10^5$ (also
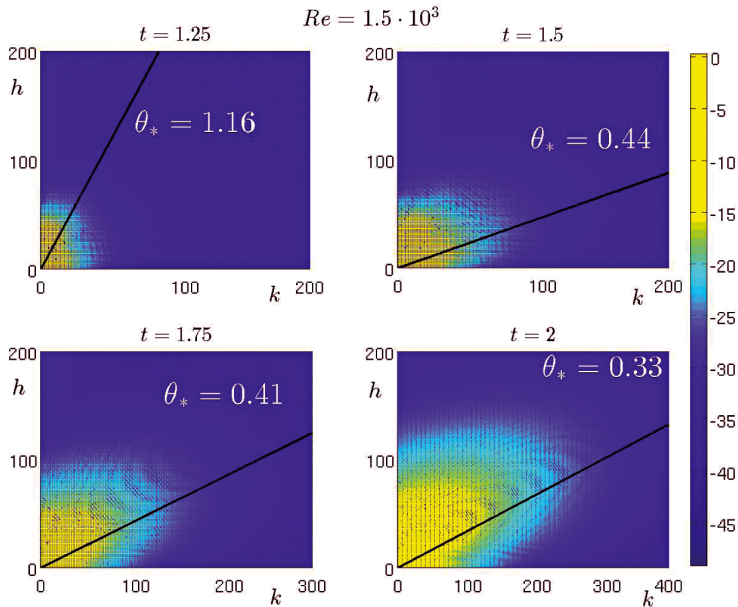

Fig. 43. The spectrum (in log-scale) of u for $Re = 1.5 \cdot 10^3$ at various time.
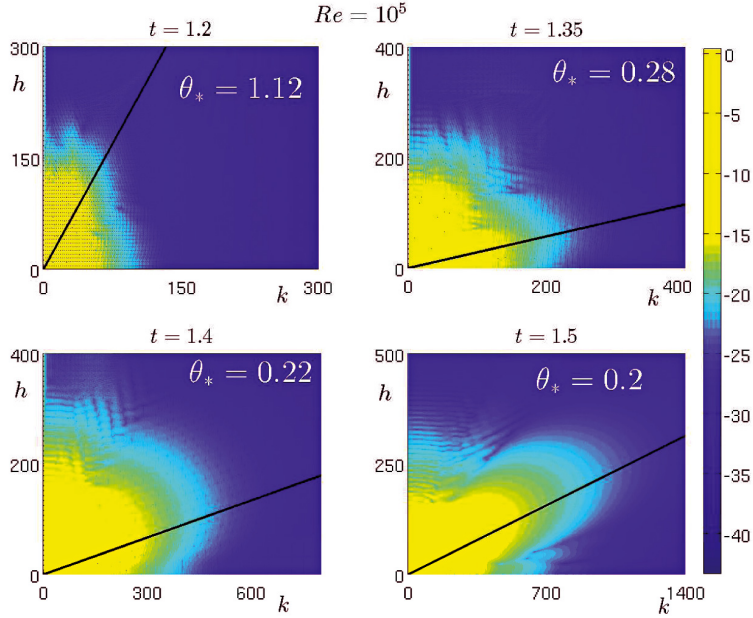
Fig. 44. The spectrum (in log-scale) of u for $Re = 10^5$ at various time. At $t \approx 1.35$, a bulge forms in the spectrum that becomes more pronounced as time passes due to the effect of the small-scale interaction characterized by appearance of strong gradients of u in the variable θ.

for $Re = 5 \cdot 10^3, 10^4, 5 \cdot 10^4$ not shown here) we can observe that the bulge begins to appear at the time in which small-scale interaction begins ($t \approx 1.35$), while for the case $Re = 1.5 \cdot 10^3$ the bulge never forms and the spectrum grows throughout a wider range around the most singular direction. We can relate the presence of this bulge to the effect of the small-scale interaction which reveals itself through the formation of large gradients in the angular direction θ in the solution, leading to the excitement of the high wavenumber Fourier modes along the most singular direction. Moreover as time passes, the most singular direction approaches $\theta^* = 0$, which confirms that the relevant gradients present in u are those relative to the coordinate θ. This result is also compatible with the result obtained for Prandtl's solution for which, at the singularity time, the most singular direction is $\theta^* = 0$.

5.3 - *KP equation*

The KP equation can be put in the form:

$$(5.8) \qquad \partial_t u + 6u\partial_x u + \epsilon^2 \partial_{xxx} u = -\lambda \partial_x^{-1} \partial_{yy} u \; ,$$
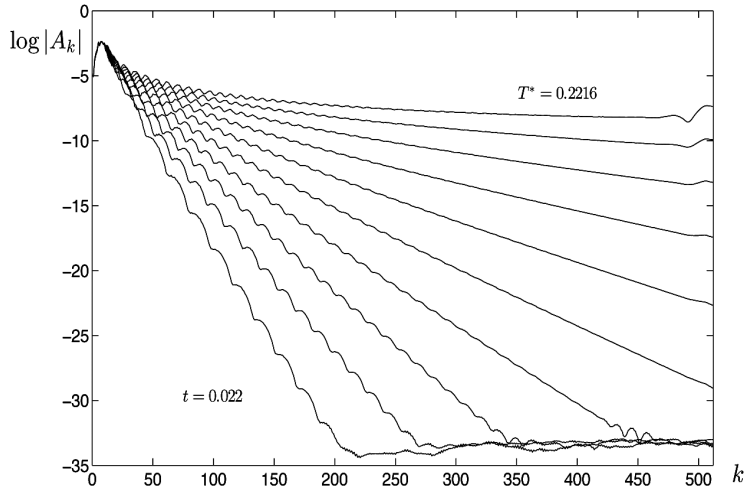
Fig. 45. The behavior in time of the shell summed amplitude up to the singularity time.

with $\lambda = \pm 1$ (here we consider the case when $\lambda = 1$ with defocusing effects) with periodic boundary condition. The variable x and y are in $[-L_x\pi, L_x\pi]$ and $[-L_y\pi, L_y\pi]$, and we choose $L_x = L_y = 5$.
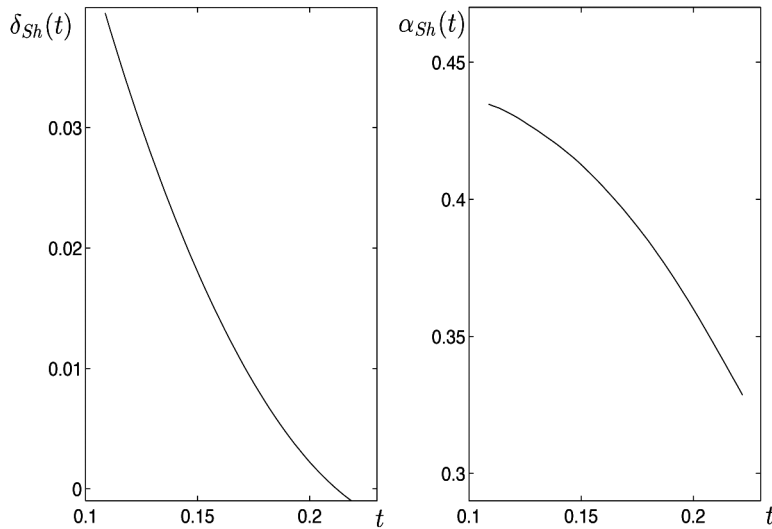

Fig. 46. The behavior in time of the width of the analyticity strip. The singularity time is $T^* \approx 0.2216$. The singularity is of cubic-root type.
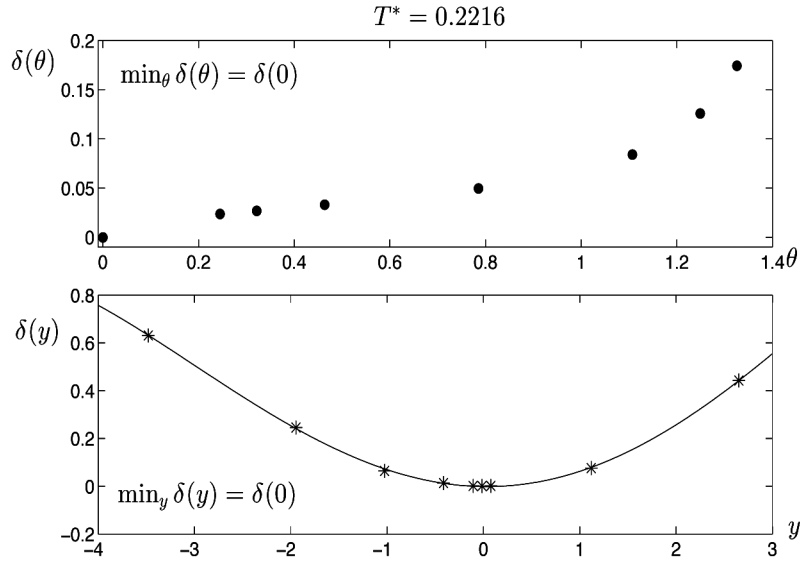
Fig. 47. The most singular direction is $\theta = 0$. If one estimates the δ in its dependence on the y variable, one finds that the location of the singularity is at $y \approx 0$.

We consider the initial datum:

$$(5.9) \qquad u(x, y, 0) = -\partial_x \text{sech}^2\left(\sqrt{x^2 + y^2}\right),$$

in such a way that the Fourier mode at $k_x = 0$ is null at the initial time and we can treat the ∂_x^{-1} as $-i/k_x$ with $k_x \neq 0$.

The analysis of the singularity formation when $\epsilon = 0$ is very similar to the Prandtl case.

In Fig. 45 we show the shell-summed amplitudes, where it is evident the loss of exponential decay. Fitting these amplitudes we get the results shown in Fig. 46, where one can see that, at the critical time $T^* = 0.2216$, the solution loses analyticity as a cubic-root singularity hits the real axis. In Fig. 47 we show the angular dependence of δ and one can see that the most singular direction is $\theta = 0$. This result allows to treat the normal variable as a parameter. At the bottom of the same Figure we show the dependence of δ on y, and one can see that $\delta(y)$ attains its minimum at $y = 0$.

In Fig. 48 we show the solution, at the singularity time, at the location $y = 0$ and in Fig. 49 it is shown the behavior in time of the spectrum at location $y = 0$. In Fig. 50 one can see the results of the singularity tracking method for the initial datum (5.9) at the location $y = 0$. The examination of the oscillatory behavior of
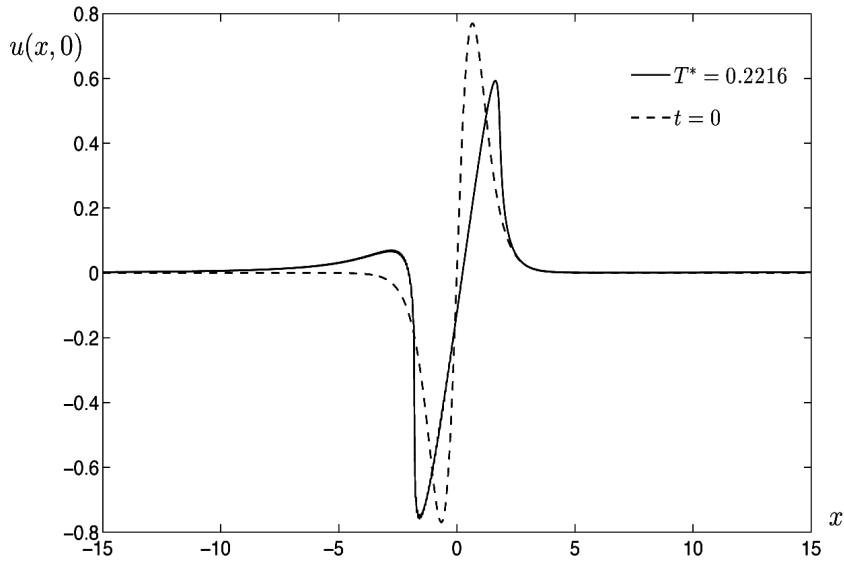
Fig. 48. The solution of the KP equation, with $\epsilon = 0$, at the location $y = 0$ for initial datum given by (5.9).

Fig. 49. The spectrum of the solution KP equation, with $\epsilon = 0$, at the location $y = 0$ for initial datum given by (5.9).
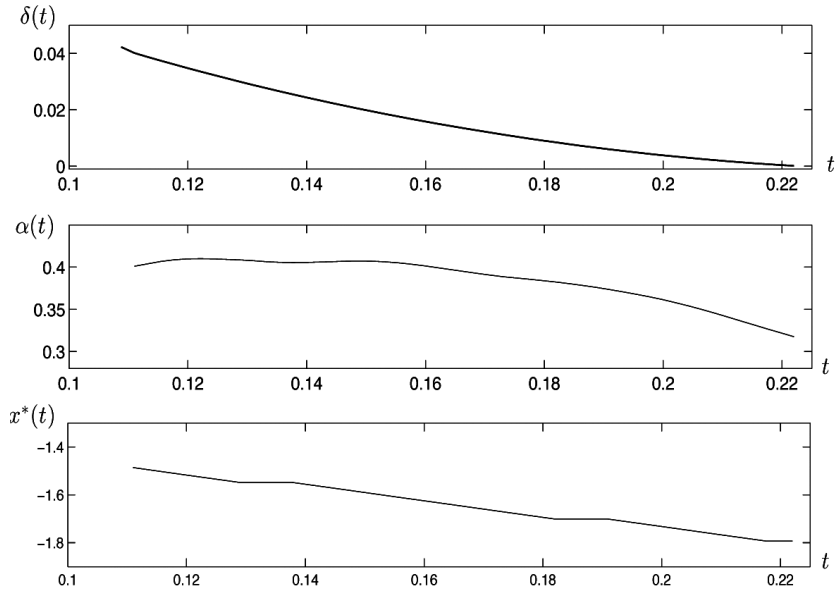
Fig. 50. The results of the singularity tracking at $y = 0$. One can see that at $t \approx 0.2216$ the strip of analyticity shrinks to zero as the result of a cubic–root singularity hitting the real axis. The location of the real coordinate of the singularity at the singularity time is $x^* \approx -1.79$.

Fig. 51. The solution of the KP equation, with $\epsilon = 0.1$, at the location $y = 0$ for initial datum given by (5.9) at three different times.
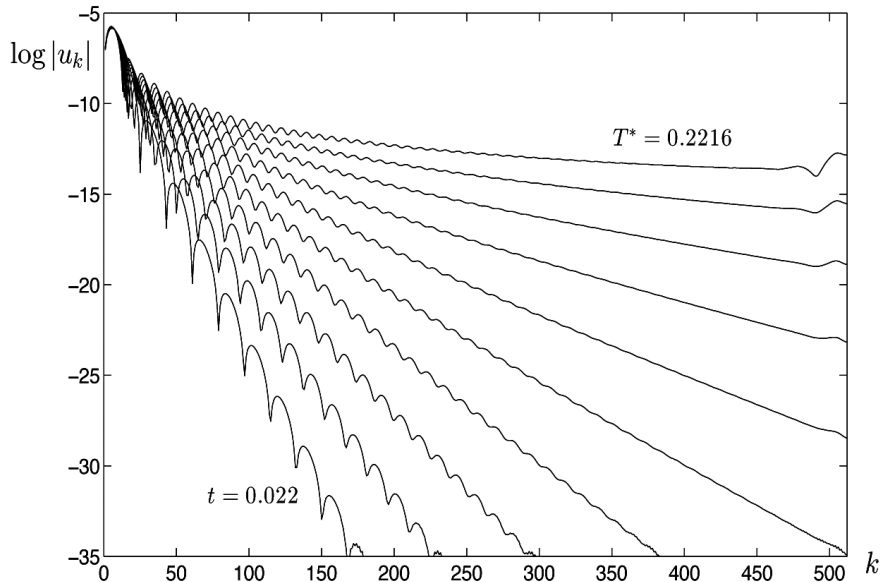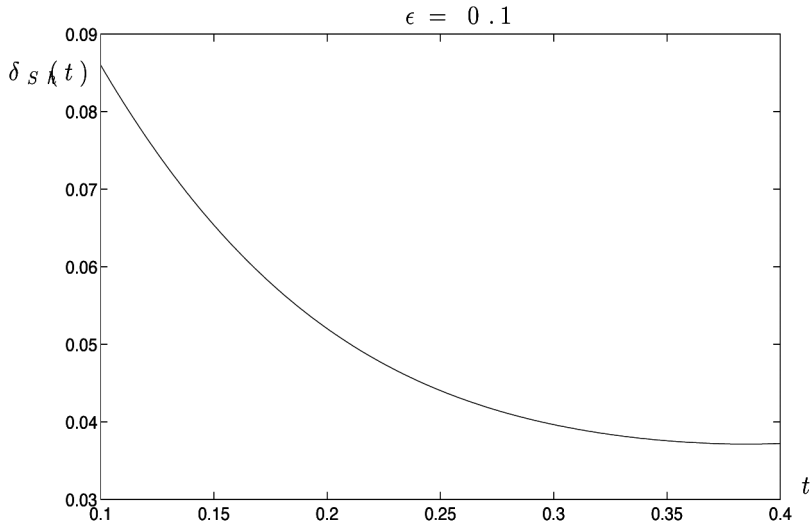
Fig. 52. The behavior in time of the width of the analyticity strip when $\epsilon = 0.1$.

the spectrum, gives the real location of the singularity; in Fig. 50 one can see that $x^* \approx -1.79$.
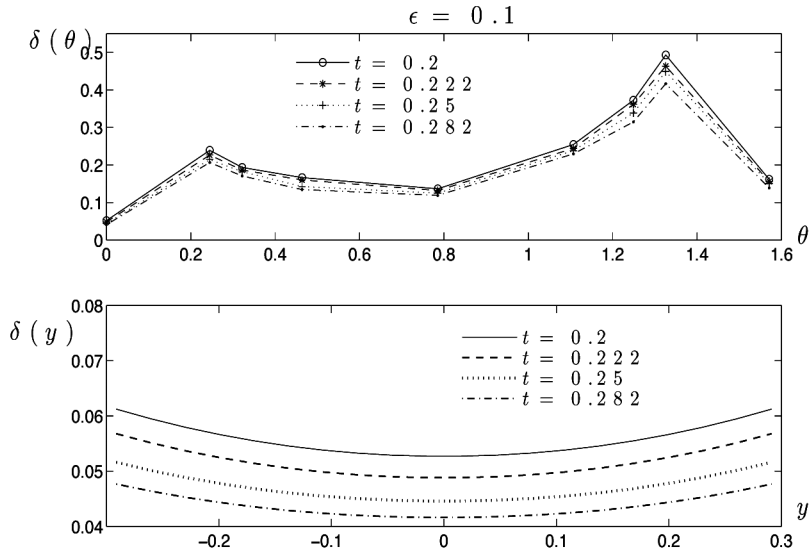
Fig. 53. The behavior of the $\delta(y)$ and $\delta(\theta)$ of the KP equation with $\epsilon = 0.1$ at different times. The most singular direction is $\theta = 0$. If one estimates the δ in its dependence on the y variable, one finds that the location of the complex singularity is at $y \approx 0$.
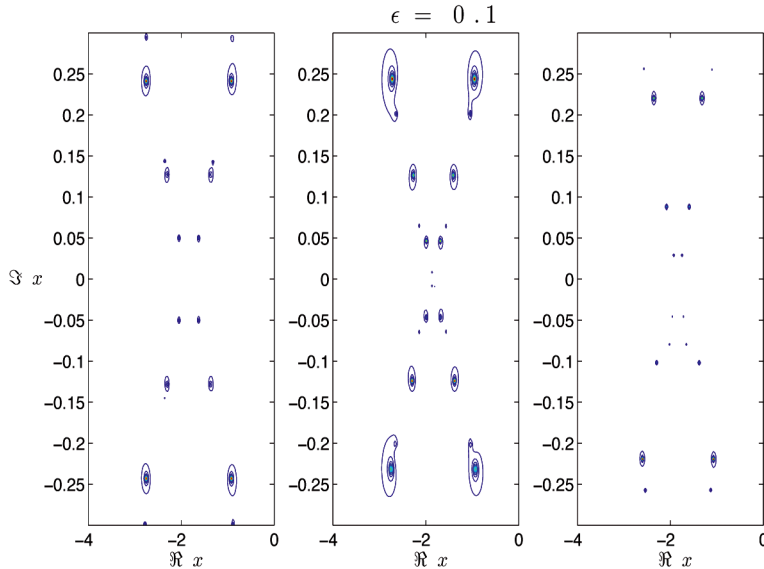
Fig. 54. Poles at different times for the solution of the KP equation, with $\epsilon = 0.1$, at the location $y = 0$. The Padé analysis results.

We consider now the KP equation with $\epsilon = 0.1$, and we want to analyze the behavior of the complex singularities. As previously observed for the KdV equations, the solution of the KP equation with $\epsilon = 0.14$ has a regions of rapid modulated oscillations in the vicinity of $x^* = -1.79$, the shock position of the dispersionless KP solution, as one can see in Fig. 51.

The analysis of the spectrum using the shell-summed amplitudes is given in Fig. 52. The behavior in time of the δ_{Sh} width of the analyticity strip shows that when $\epsilon = 0.1$ there is no formation of real singularity.

In Fig. 53 we show the angular dependence of δ at different times and one can see that the most singular direction is $\theta = 0$. This result allows to treat the normal variable as a parameter. At the bottom of the same figure we show the dependence of δ on y, and one can see that $\delta(y)$ attains its minimum at $y = 0$.
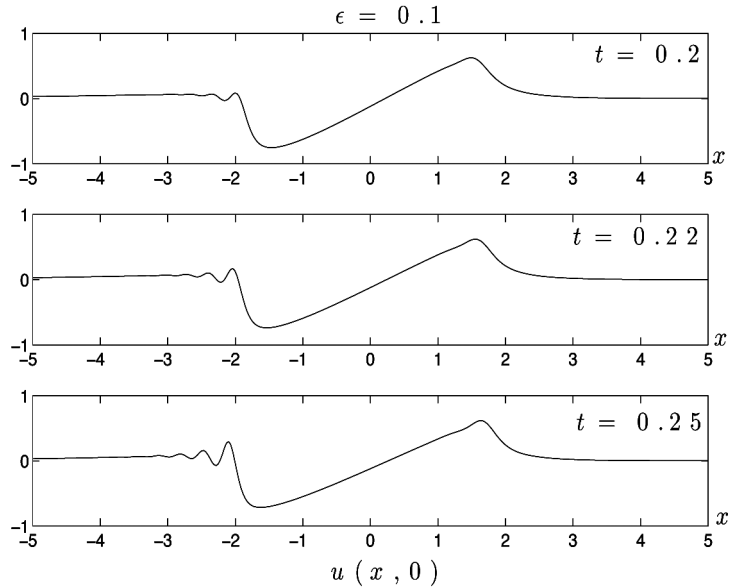
We compute the Padé approximants for the solution of the KP equation, with $\epsilon = 0.1$, at the location $y = 0$ for initial datum given by (5.9) at three different times (see Fig. 54). We observe a behavior very similar to what observed for the dispersive Burgers equation and the KdV equation. We conjecture that the region of modulated oscillations in the vicinity of the shocks in the dispersionless solution of a nonlinear dispersive equation can be explained with the presence of coalescing complex singularities located on a curve (maybe a straight line) which approaches the real axis.

5.4 - *Vortex layers*

In this section we shall apply the singularity tracking method to analyze the complex singularities for a viscous vortex layer whose solution is governed by the Navier-Stokes equation. Vortex layers have been extensively studied from both a theoretical and numerical point of view. Moore in [**51**] analyzed the effect of the thickness on the motion of the layer in the case of a vorticity of constant strength; in [**49**] the authors proved that the dynamics of a vortex layer of constant strength converges to the dynamics of a vortex sheet when the thickness of the layer goes to zero. In [**9**] the authors considered the case in which the vorticity is non uniform and concentrated on a small layer, and they derived the equations ruling the flow inside the layer, proving the well posedness of these equation. In the limit of the thickness of the layer going to zero, the vortex layer motion can be viewed as a regularization of the vortex-sheet motion. It is well known that a perturbed sheet develops a mechanism similar to the Kelvin-Helmholtz instability, leading to the ill posedness of the Birkhoff-Rott equation, which rules the vortex-sheet dynamics, and to a curvature singularity. This was firstly proved analytically by Moore ([**52, 53**]) which performed a small amplitude perturbation on the Birkhoff-Rott equation; his analysis indicated the presence of branch singularities of order 3/2 hitting the real axis in finite time. Moore's results were supported by the analysis presented in [**5**], by the rigorous results in [**23, 8**], and by direct numerical simulations ([**66, 44, 20**]). Further, numerical solutions of models invoking regularization agents such as finite-sheet thickness ([**51, 3**]), blobs ([**2**]) or viscosity ([**72, 15**]), have been found to converge to the vortex-sheet solution at times before a singularity forms in the vortex-sheet model, and allows to continue the vortex-sheet solution after singularity time; however, the inclusion of viscous term in the Birkhoff-Rott equation, which lead to Dhanak's model ([**22**]) does not necessarily prevent the singularity formation ([**68**]).

Here we perform the complex singularity analysis on a vortex layer of small thickness, in which the regularizing effect of the viscosity is included. The singularity formation is prevented, although some typical features like the roll-up of the vortex layer in a cat's eye type spiral are preserved.

We consider an incompressible 2D viscous flow in which the initial vorticity is concentrated on a layer of thickness $\epsilon = \sqrt{\nu}$, being ν the viscosity of the flow, and outside the layer the flow is irrotational. Namely, the initial vorticity distribution can be expressed as

$$\omega_0(x, y) = \int_D f_\epsilon(\xi, \eta)\delta(x - \xi, \phi(x) - \eta)d\xi d\eta,$$

where $(x, \phi(x))$ is the curve along which we build the layer, $f_\epsilon(x, y)$ is a regular function having as support the layer, δ is the Dirac function, and $D = [0, 2\pi] \times [0, 2\pi]$ is the periodic domain in which the problem is defined. We choose f_ϵ so that $\lim_{\epsilon \to 0, \omega_0 \to \infty} (\epsilon \omega_0)$ is finite, and with this condition in the inviscid limit $\epsilon \to 0$ the velocity across the vortex-sheet curve $(x, \phi(x))$ experiences a jump discontinuity.

The governing equations for the flow evolution are the NS equations, which read in the vorticity-streamfunction formulation as:

$$\partial_t \omega + u \partial_x \omega + v \partial_y \omega = \nu(\partial_{xx}^2 \omega + \partial_{yy}^2 \omega), \tag{5.10}$$

$$\partial_{xx}^2 \psi + \partial_{yy}^2 \psi = -\omega, \tag{5.11}$$

$$u = \partial_y \psi, \quad v = -\partial_x \psi, \tag{5.12}$$

$$\omega(\theta, r, t = 0) = \omega_0(x, y), \tag{5.13}$$

$$\phi(x) = \pi - \sin(x)/8, \tag{5.14}$$

$$f_\epsilon(x, y) = -\sqrt{2\pi} \exp\left(-(y^2/(2\epsilon^2))\right)/\epsilon. \tag{5.15}$$

Equation (5.10) is the vorticity-transport equation, (5.11) is the Poisson equation for the streamfunction, and equations (5.12) relate the velocity components to the streamfunction. The initial condition is given by (5.13), (5.14) and (5.15), which express an highly concentrated negative vorticity on a small sinusoidal layer having thickness of order $\sqrt{\nu}$ along the y-direction. The problem is solved in D by imposing periodic boundary conditions for both the tangential and normal variable, and a fully spectral numerical scheme is used with a third order semi-implicit Runge-Kutta scheme as temporal discretization.

5.4.1 - Roll-up process and small-scale phenomena

The dynamics of the vorticity, at different ν, is shown in Figs. 55–57. In all cases the typical roll-up into a spiral precess is visible, although we can observe two different regimes depending on the viscosity. For $\nu = 10^{-2}$ during the roll-up process there is always a big core of negative vorticity with center in (π, π), while for $\nu = 10^{-3}, 10^{-4}$ a pair of negative vortex cores, connected by a thin braid of vorticity, forms (these cores are visible in Fig. 56c and Fig. 57b). Notice that as $\nu \to 0$, our initial is datum is the same used by Moore [51] for which it is well known that a pair of curvature singularities, symmetric with respect to π, appears in the vortex sheet curve (see also [20]). Here the regularizing effect of the viscous layer prevents the pair of singularities to become real, but the two cores actually form where the curvature singularities should be. As time passes each core rotates under the effect of the velocity field induced by the other core, leading to their pairing (Fig. 56d and Fig. 57d). For $\nu = 10^{-4}$ the flow evolution is even more chaotic with the formation of several small vortical structures during the roll-up process. This different flow

(a) $\nu = 10^{-2}, t = 0.5$

(b) $\nu = 10^{-2}, t = 1.1$

(c) $\nu = 10^{-2}, t = 1.9$

(d) $\nu = 10^{-2}, t = 3$

Fig. 55. The vorticity distribution at various time for $\nu = 10^{-2}$. The roll up behavior typical of the vortex sheet motion is visible.

evolution for the various viscosities reveals the presence of a small-scale regime for moderate-low viscosity, similarly to what observed for a viscous boundary layer flow (see previous section 5.2), where for moderate-high Re number a small-scale inter-action develops . In a boundary layer flow, this interaction is characterized by the same small-scale vortical structures formation observed in the roll-up process of the vortex layer, although it is ruled by a different physical mechanism (the unsteady

(a) $\nu = 10^{-3}, t = 0.5$

(b) $\nu = 10^{-3}, t = 0.85$
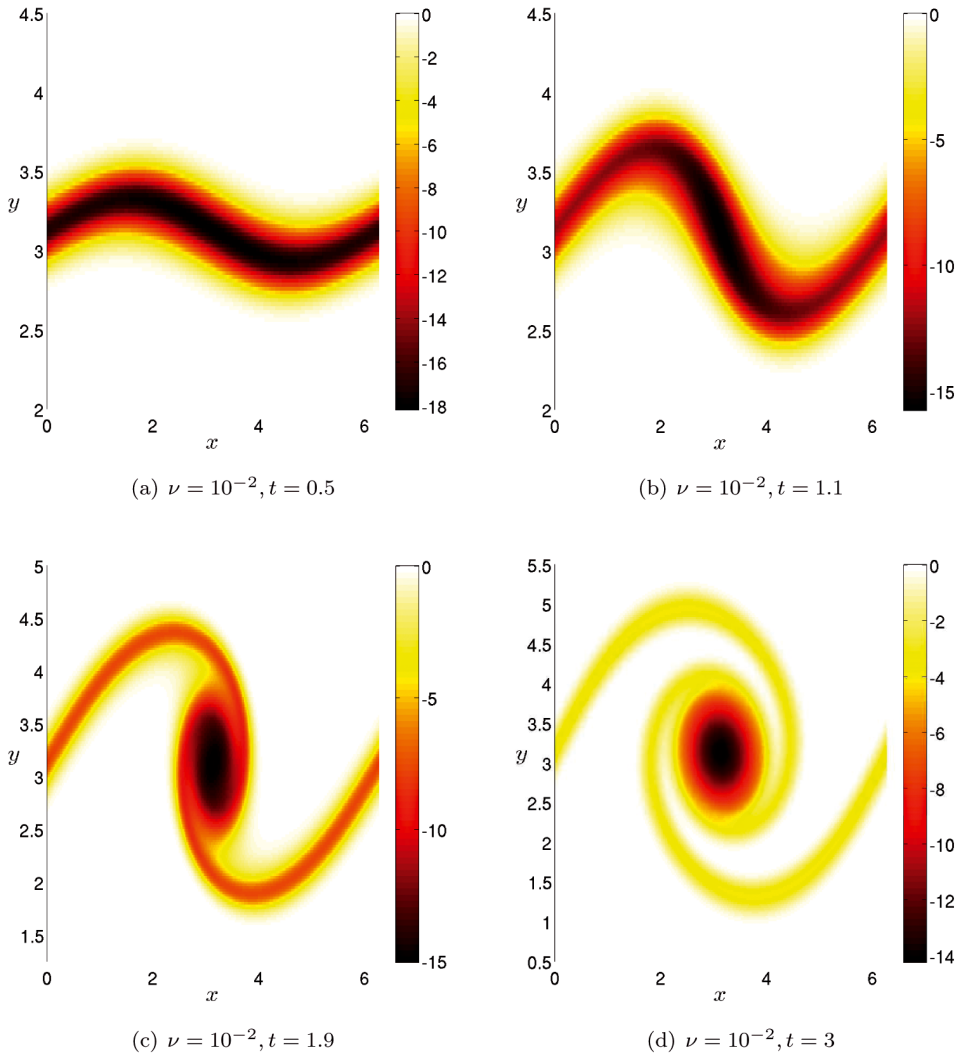
(c) $\nu = 10^{-3}, t = 1.1$
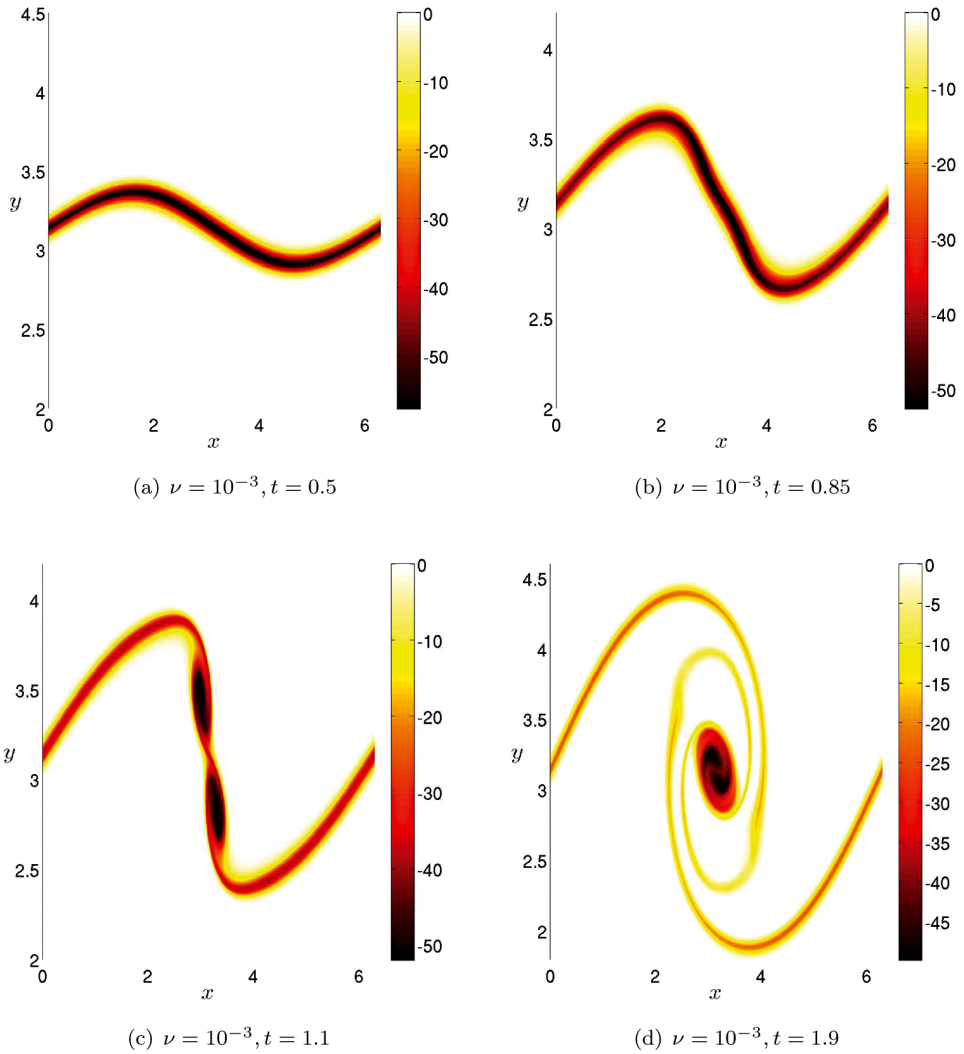
(d) $\nu = 10^{-3}, t = 1.9$

Fig. 56. The vorticity distribution at various time for $\nu = 10^{-3}$. The roll up behavior typical of the vortex sheet motion is visible. With respect to the case $\nu = 10^{-2}$ a pair of vorticity cores forms which eventually collapse on each other forming a big core visible at time $t = 1.9$.

separation process). In [**17, 43, 30, 31, 32**] it was also shown that the small-scale interaction was characterized by the presence of several peaks in the time evolution of the enstrophy and the palinstrophy of the flow, here defined as $\Omega = \|\omega\|^2_{L^2(D)}$ and $P = \|\nabla\omega\|^2_{L^2(D)}$ respectively. We observe, for the vortex layer solution, the presence of peaks for $\nu = 10^{-3}, 10^{-4}$ only in the time evolution of P, as one can see in Fig. 59, while Ω always decreases due to the fact that there is no vorticity production as one

(a) $\nu = 10^{-4}, t = 0.7$

(b) $\nu = 10^{-4}, t = 0.85$

(c) $\nu = 10^{-4}, t = 1.2$
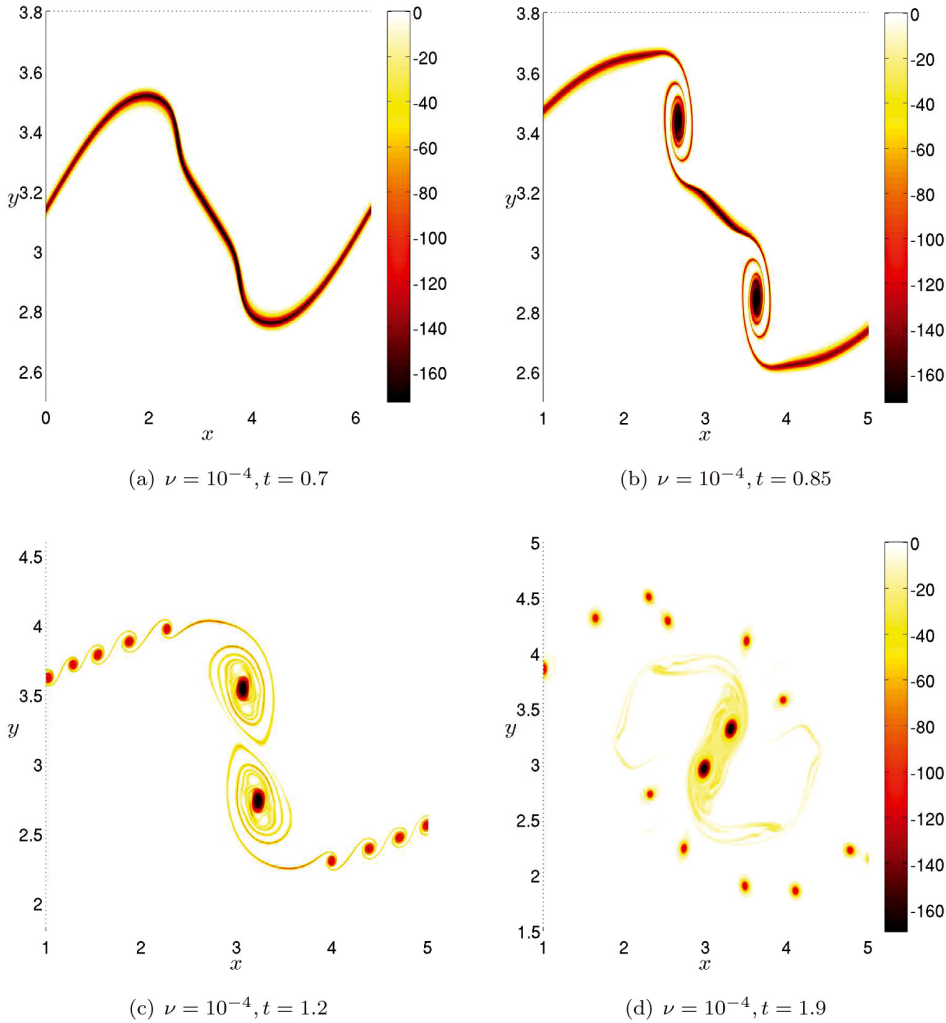
(d) $\nu = 10^{-4}, t = 1.9$

Fig. 57. The vorticity distribution at various time for $\nu = 10^{-4}$. As observed for $\nu = 10^{-3}$, a pair of vorticity cores form, and during the roll-up process several other spiral vortexes form in cascade.

can see from the enstrophy equation on a periodic domain $\dfrac{d\Omega}{dt} = -2\nu P.$ [1] It is worth noting that the first growth of the palinstrophy (after $t \approx 0.95$ and $t \approx 0.7$ for $\nu = 10^{-3}$ and $\nu = 10^{-4}$ respectively) happens just after the formation of the pair of vortex cores. For $\nu = 10^{-2}$ we have checked up to time $t = 30$ that palinstrophy never

---

[1] For a boundary layer flow the enstrophy equation also contains a term depending on the vorticity production which is able to increase in time the enstrophy.
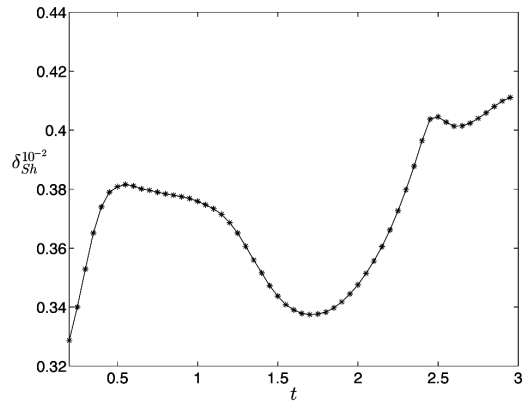
(a) Time evolution of $\delta_{Sh}^{10^{-2}}$.
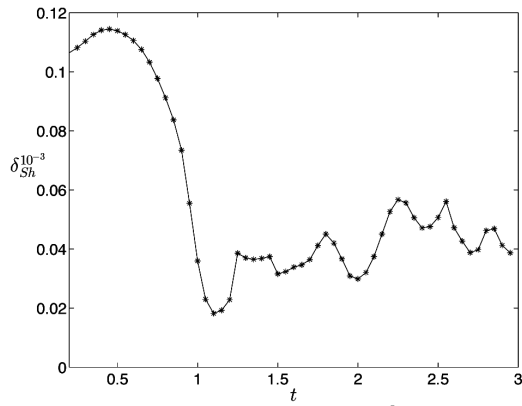
(b) Time evolution of $\delta_{Sh}^{10^{-3}}$.
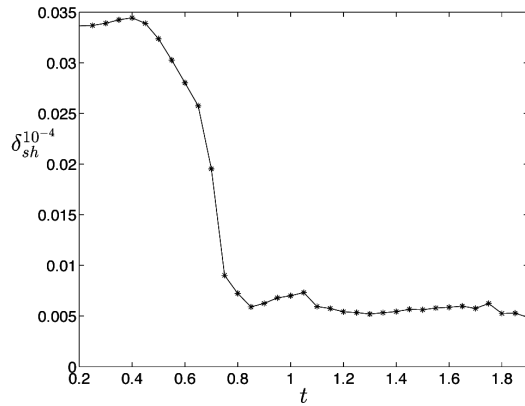
(c) Time evolution of $\delta_{Sh}^{10^{-4}}$.

Fig. 58. Time evolution of the width of analyticity of the viscous vortex layer solutions for different viscosities.
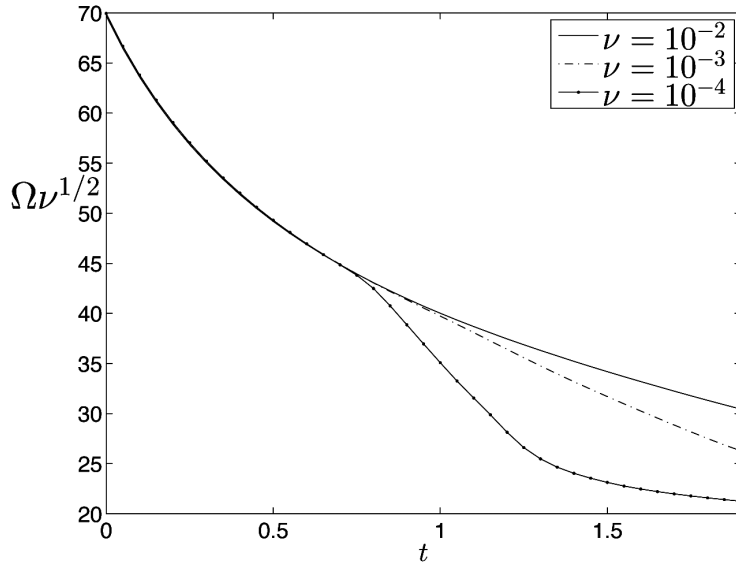
(a) The enstrophy Ω time evolution. Ω is scaled by a factor $\nu^{1/2}$ so that all the quantities have the same order.
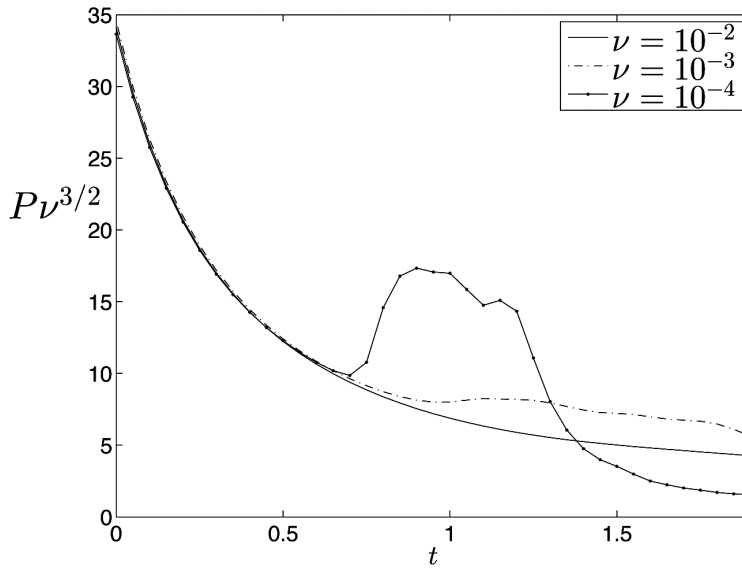
(b) The palinstrophy P time evolution. P is scaled by a factor $\nu^{3/2}$ so that all the quantities have the same order.

Fig. 59. For $\nu = 10^{-3}, 10^{-4}$ the palinstrophy increases in time due to the formation of a pair of vorticity cores close to (π, π) (see Figs. 56-57). For $\nu = 10^{-2}$ there is no peaks in the palinstrophy, and during the roll-up process of the vortex layer the vorticity forms a big patch centered in (π, π) (see Fig. 55).

increases, and the big core of negative vorticity never splits, which confirms that the small-scale regime is not visible for high viscosity value.

5.4.2 - Singularity tracking for the vortex layer

We now look for complex singularities in the solution of the Navier-Stokes with vortex layer initial datum. In particular we compute the shell-summed Fourier amplitudes A_K of the streamfunction

$$\psi(x, y, t) = \sum_{k_1, k_2} \psi_{k_1 k_2}(t) e^{ik_1 x} e^{ik_2 y}$$

and we apply the fitting procedures to obtain the rate of exponential decay δ_{Sh}^v and the rate of algebraic decay α_{Sh}^v from (5.3). The time evolution of $\delta_{Sh}^v(t)$ is shown in Figs. 58a-c. In all cases the $\delta_{Sh}^v(t)$ reaches a first minimum value at $t_m \approx 1.7, 1.1, 0.85$ for $v = 10^{-2}, 10^{-3}, 10^{-4}$. Even if it is quite difficult to determine the physical counterpart related to the formation of this minimum we have observed that at t_m the
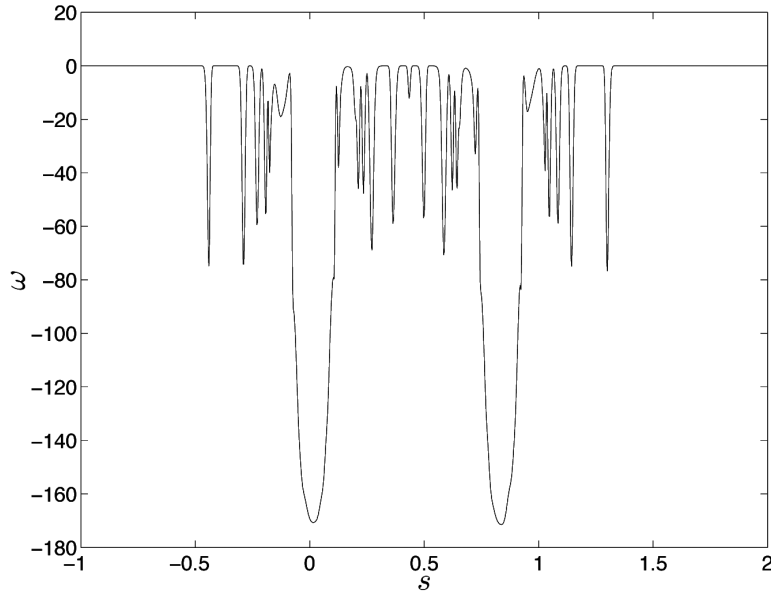
Fig. 60. The cut of the vorticity for $v = 10^{-4}$ at $t = 1.2$ along the line $r(s) = \tan(1.378)(s - 3.068) + 3.559$. This line connects the centers of the two cores of negative vorticity located at $(3.068, 3.559)$ and $(3.227, 2.737)$ (see Fig. 57c). Along r the vorticity experiences an eruptive behavior, which is also suggested by the presence of a 3/2-singularity retrieved by singularity tracking method applied to the streamfunction ψ.

upper and lower flow portions, originally separated by the thin layer, begin to protrude into the other portion and to curl back on themselves forming the typical spiral shape in the vorticity distribution.

Regarding the characterization of the singularity, which is obtained by determining the rate of algebraic decay α_{Sh}^{v} of the shell-summed Fourier amplitudes, we have obtained through a numerical fitting that $\alpha_{Sh}^{v} \approx 3/2$ for all v; this means that the main complex singularity of the streamfunction is a $3/2$-singularity which reveals an eruptive behavior of the streamfunction second derivatives. This is somewhat expected, as the second derivatives of the streamfunction are related to the vorticity which is highly concentrated and shows an eruptive behavior along the thin layer. This can be seen, for instance, by looking in Fig. 60 at the cut of the vorticity along the line connecting the two cores of vorticity at time $t = 1.2$ for $v = 10^{-4}$ (we varies this line $r(s)$ along the parameter s having origin in the center of the upper core located in $(3.068, 3.559)$.): the vorticity experiences an eruptive behavior in correspondence to the thin vorticity filaments wrapping the two cores.

References

[1]   G. R. BAKER, R. E. CAFLISCH and M. SIEGEL, *Singularity formation during Rayleigh-Taylor instability*, J. Fluid Mech. **252** (1993), 51-75.

[2]   G. R. BAKER and L. D. PHAM, *A comparison of blob methods for vortex sheet roll-up*, J. Fluid Mech. **547** (2006), 297-316.

[3]   G. R. BAKER and M. J. SHELLEY, *On the connection between thin vortex layers and vortex sheets*, J. Fluid Mech. **215** (1990), 161-194.

[4]   G. A. BAKER JR. and P. GRAVES-MORRIS, *Padé approximants*, 2nd ed., Cambridge University Press, Cambridge 1996.

[5]   G. R. BAKER, D. I. MEIRON and S. A. ORSZAG, *Generalized vortex methods for free-surface flow problems*, J. Fluid Mech. **123** (1982), 477-501.

[6]   J. P. BOYD, *Large-degree asymptotics and exponential asymptotics for Fourier, Chebyshev and Hermite coefficients and Fourier transforms*, J. Engrg. Math. **63** (2009), no. 2-4, 355-399.

[7]   J. P. BOYD, *Chebyshev and Fourier spectral methods*, Dover Publications, Mineoal, New York 2001.

[8]   R. E. CAFLISCH and O. F. ORELLANA, *Singular solutions and ill-posedness for the evolution of vortex sheets*, SIAM J. Math. Anal. **20** (1989), no. 2, 293-307.

[9]   R. E. CAFLISCH and M. SAMMARTINO, *Vortex layers in the small viscosity limit*, "WASCOM 2005"—13th Conference on Waves and Stability in Continuous Media, World Sci. Publ., Hackensack, NJ 2006, pp. 59-70.

[10]   R. E. CAFLISCH and M. SIEGEL, *A semi-analytic approach to Euler singularities*, Methods Appl. Anal. **11** (2004), no. 3, 423-430.

[11]   R. E. CAFLISCH, *Singularity formation for complex solutions of the 3D incompressible Euler equations*, Phys. D **67** (1993), 1-18.

[12]   R. E. CAFLISCH, S. JIN and G. RUSSO, *Uniformly accurate schemes for hyperbolic systems with relaxation*, SIAM J. Numer. Anal. **34** (1997), no. 1, 246-281.

[13]   C. CANUTO, M. Y. HUSSAINI, A. QUARTERONI and T. A. ZANG, *Spectral methods*, Fundamentals in single domains, Scientific Computation, Springer-Verlag, Berlin 2006.

[14]   G. F. CARRIER, M. KROOK and C. E. PEARSON, *Functions of a complex variable. Theory and technique*, McGraw-Hill Book Co., New York-Toronto, Ont.-London 1966.

[15]   M. J. CHEN and L. K. FORBES, *Accurate methods for computing inviscid and viscous Kelvin-Helmholtz instability*, J. Comput. Phys. **230** (2011), no. 4, 1499-1515.

[16]   C. CICHOWLAS and M.-E. BRACHET, *Evolution of complex singularities in Kida-Pelz and Taylor-Green inviscid flows*, Fluid Dynam. Res. **36** (2005), 239-248.

[17]   H. J. H. CLERCX and C.-H. BRUNEAU, *The normal and oblique collision of a dipole with a no-slip boundary*, Computers & Fluids **35** (2006), no. 3, 245-279.

[18]   G. M. COCLITE, F. GARGANO and V. SCIACCA, *Analytic solutions and singularity formation for the Peakon b-family equations*, Acta Appl. Math. **122** (2012), 419-434.

[19]   S. J. COWLEY, *Computer extension and analytic continuation of Blasius' expansion for impulsively flow past a circular cylinder*, J. Fluid Mech. **135** (1983), 389-405.

[20]   S. J. COWLEY, G. R. BAKER and S. TANVEER, *On the formation of Moore curvature singularities in vortex sheets*, J. Fluid Mech. **378** (1999), 233-267.

[21]   G. DELLA ROCCA, M. C. LOMBARDO, M. SAMMARTINO and V. SCIACCA, *Singularity tracking for Camassa-Holm and Prandtl's equations*, Appl. Numer. Math. **56** (2006), no. 8, 1108-1122.

[22]   M. R. DHANAK, *Equation of motion of a diffusing vortex sheet*, J. Fluid Mech. **269** (1994), 265-281.

[23]   J. DUCHON and R. ROBERT, *Global vortex sheet solutions of Euler equations in the plane*, J. Differential Equations **73** (1988), no. 2, 215-224.

[24]   N. M. ERCOLANI, C. D. LEVERMORE and T. ZHANG, *The behavior of the Weyl function in the zero-dispersion KdV limit*, Comm. Math. Phys. **183** (1997), no. 1, 119-143.

[25]   N. M. ERCOLANI, I. R. GABITOV, C. D. LEVERMORE and D. SERRE, (eds.), *Singular limits of dispersive waves*, NATO Advanced Science Institutes Series B: Physics, **320**, Plenum Press, New York 1994.

[26]   J.-D. FOURNIER and U. FRISCH, *L'équation de Burgers déterministe et statistique*, J. Méc. Théor. Appl. **2** (1983), no. 5, 699-750.

[27]   U. FRISCH, T. MATSUMOTO and J. BEC, *Singularities of Euler flow? Not out of the blue!*, J. Statist. Phys. **113** (2003), 761-781.

[28]   F. GARGANO, M. C. LOMBARDO, M. SAMMARTINO and V. SCIACCA, *Singularity formation and separation phenomena in boundary layer theory*, Partial

differential equations and fluid mechanics, London Math. Soc. Lecture Note Ser., **364**, Cambridge Univ. Press, Cambridge 2009, pp. 81-120.

[**29**]   F. GARGANO, M. SAMMARTINO and V. SCIACCA, *Singularity formation for Prandtl's equations*, Phys. D **238** (2009), no. 19, 1975-1991.

[**30**]   F. GARGANO, M. SAMMARTINO and V. SCIACCA, *High Reynolds number Navier-Stokes solutions and boundary layer separation induced by a rectilinear vortex*, Computers & Fluids **52** (2011), 73-91.

[**31**]   F. GARGANO, M. SAMMARTINO, V. SCIACCA and K. W. CASSEL, *Analysis of complex singularities in high-Reynolds-number Navier-Stokes solutions*, J. Fluid Mech. **747** (2014), 381-421.

[**32**]   —, *Viscous-inviscid interactions in a boundary-layer flow induced by a vortex array*, Acta Appl. Math. **132** (2014), 295-305.

[**33**]   R. E. GOLDSTEIN, A. I. PESCI and M. J. SHELLEY, *Instabilities and singularities in Hele–Shaw flow*, Phys. Fluids **10** (1998), no. 11, 2701-2723.

[**34**]   T. GRAVA and C. KLEIN, *A numerical study of the small dispersion limit of the Korteweg-de Vries equation and asymptotic solutions*, Phys. D **241** (2012), no. 23-24, 2246-2264.

[**35**]   A. J. GUTTMANN, *Asymptotic analysis of power-series expansions*, Phase transitions and critical phenomena, Vol. 13, Academic Press, London 1989, pp. 1-234.

[**36**]   A. HARTEN, *High resolution schemes for hyperbolic conservation laws*, J. Comput. Phys. **49** (1983), no. 3, 357-393.

[**37**]   P. HENRICI, *Applied and computational complex analysis, vol i, ii & iii*, Wiley-Interscience Publication, John Wiley & Sons, New York 1993.

[**38**]   S. JIN, C. D. LEVERMORE and D. W. MCLAUGHLIN, *The semiclassical limit of the defocusing NLS hierarchy*, Comm. Pure Appl. Math. **52** (1999), no. 5, 613-654.

[**39**]   S. KAMVISSIS, K. D. T.-R. MCLAUGHLIN and P. D. MILLER, *Semiclassical soliton ensembles for the focusing nonlinear Schrödinger equation*, Annals of Mathematics Studies, **154**, Princeton University Press, Princeton, NJ 2003.

[**40**]   S. KIDA, *Study of complex singularities by filtered spectral method*, J. Phys. Soc. Japan **55** (1986), no. 5, 1542-1555.

[**41**]   C. KLEIN and K. ROIDOT, *Numerical study of shock formation in the dispersion-less Kadomtsev-Petviashvili equation and dispersive regularizations*, Phys. D **265** (2013), 1-25.

[**42**]   —, *Numerical study of the semiclassical limit of the Davey-Stewartson II equations*, Nonlinearity **27** (2014), no. 9, 2177-2214.

[**43**]   W. KRAMER, H. J. H. CLERCX and G. J. F. VAN HEIJST, *Vorticity dynamics of a dipole colliding with a no-slip wall*, Phys. Fluids **19** (2007), 126603.

[**44**]   R. KRASNY, *A study of singularity formation in a vortex sheet by the point-vortex approximation*, J. Fluid Mech. **167** (1986), 65-93.

[**45**]   P. D. LAX and C. D. LEVERMORE, *The small dispersion limit of the Korteweg-de Vries equation. I*, Comm. Pure Appl. Math. **36** (1983), no. 3, 253-290.

[**46**]   —, *The small dispersion limit of the Korteweg-de Vries equation. II*, Comm. Pure Appl. Math. **36** (1983), no. 5, 571-593.

[**47**]   —, *The small dispersion limit of the Korteweg-de Vries equation. III*, Comm. Pure Appl. Math. **36** (1983), no. 6, 809-829.

[48]   K. MALAKUTI, R. E. CAFLISCH, M. SIEGEL and A. VIRODOV, *Detection of complex singularities for a function of several variables*, IMA J. Appl. Math. **78** (2013), no. 4, 714-728.

[49]   C. MARCHIORO and M. PULVIRENTI, *Mathematical theory of incompressible nonviscous fluids*, Applied Mathematical Sciences, **96**, Springer-Verlag, New York 1994.

[50]   T. MATSUMOTO, J. BEC and U. FRISCH, *The analytic structure of 2D Euler flow at short times*, Fluid Dynam. Res. **36** (2005), no. 4-6, 221-237.

[51]   D. W. MOORE, *The equation of motion of a vortex layer of small thickness*, Studies in Appl. Math. **58** (1978), no. 2, 119-140.

[52]   —, *The spontaneous appearance of a singularity in the shape of an evolving vortex sheet*, Proc. Roy. Soc. London Ser. A **365** (1979), no. 1720, 105-119.

[53]   D. W. MOORE, *Numerical and analytical aspects of Helmholtz instability*, Theoretical and applied mechanics (Lyngby, 1984), North-Holland, Amsterdam 1985, pp. 263-274.

[54]   A. V. OBABKO and K. W. CASSEL, *Navier-Stokes solutions of unsteady separation induced by a vortex*, J. Fluid Mech. **465** (2002), 99-130.

[55]   A. V. OBABKO and K. W. CASSEL, *On the ejection-induced instability in Navier-Stokes solutions of unsteady separation*, Philos. Trans. R. Soc. Lond. Ser. A Math. Phys. Eng. Sci. **363** (2005), no. 1830, 1189-1198.

[56]   S. OSHER and S. CHAKRAVARTHY, *High resolution schemes and the entropy condition*, SIAM J. Numer. Anal. **21** (1984), no. 5, 955-984.

[57]   W. PAULS and U. FRISCH, *A Borel transform method for locating singularities of Taylor and Fourier series*, J. Stat. Phys. **127** (2007), no. 6, 1095-1119.

[58]   W. PAULS, T. MATSUMOTO, U. FRISCH and J. BEC, *Nature of complex singularities for the 2D Euler equation*, Phys. D **219** (2006), no. 1, 40-59.

[59]   M. C. PUGH and M. J. SHELLEY, *Singularity formation in thin jets with surface tension*, Comm. Pure Appl. Math. **51** (1998), no. 7, 733-795.

[60]   P. L. ROE, *Numerical algorithms for rhe linear wave equation*, Royal Aircraft Establishment Technical Report (1981), 81047.

[61]   K. ROIDOT and N. MAUSER, *Numerical study of the transverse stability of NLS soliton solution in several classes of NLS-type equations*, arxiv:1401.5349 (2014).

[62]   H. SCHLICHTING, *Boundary layer theory*, Translated by J. Kestin, 4th ed., McGraw-Hill Series in Mechanical Engineering, McGraw-Hill Book Co., New York, 1960.

[63]   D. SENOUF, R. CAFLISCH and N. ERCOLANI, *Pole dynamics and oscillations for the complex Burgers equation in the small-dispersion limit*, Nonlinearity **9** (1996), no. 6, 1671-1702.

[64]   D. SENOUF, *Dynamics and condensation of complex singularities for Burgers' equation. I*, SIAM J. Math. Anal. **28** (1997), no. 6, 1457-1489.

[65]   —, *Dynamics and condensation of complex singularities for Burgers' equation. II*, SIAM J. Math. Anal. **28** (1997), no. 6, 1490-1513.

[66]   M. J. SHELLEY, *A study of singularity formation in vortex–sheet motion by a spectrally accurate vortex method*, J. Fluid. Mech. **244** (1992), 493-526.

[67]   M. SIEGEL and R. E. CAFLISCH, *Calculation of complex singular solutions to the 3D incompressible Euler equations*, Phys. D **238** (2009), no. 23-24, 2368-2379.

[68]   S.-I. Sohn, *Singularity formation and nonlinear evolution of a viscous vortex sheet model*, Phys. Fluids **25** (2013), no. 1, 014106.

[69]   C. Sulem, P.-L. Sulem and H. Frisch, *Tracing complex singularities with spectral methods*, J. Comput. Phys. **50** (1983), no. 1, 138-161.

[70]   P. K. Sweby, *High resolution schemes using flux limiters for hyperbolic conservation laws*, SIAM J. Numer. Anal. **21** (1984), no. 5, 995-1011.

[71]   A. Tovbis, S. Venakides and X. Zhou, *On semiclassical (zero dispersion limit) solutions of the focusing nonlinear Schrödinger equation*, Comm. Pure Appl. Math. **57** (2004), no. 7, 877-985.

[72]   G. Tryggvason, W. J. A. Dahm and K. Sbeih, *Fine structure of vortex sheet rollup by viscous and inviscid simulation*, J. Fluids Eng. **113** (1991), no. 1, 31-36.

[73]   J. van der Hoeven, *On asymptotic extrapolation*, J. Symbolic Comput. **44** (2009), no. 8, 1000-1016.

[74]   L. L. van Dommelen and S. F. Shen, *The spontaneous generation of the singularity in a separating laminar boundary layer*, J. Comput. Phys. **38** (1980), 125-140.

[75]   B. van Leer, *Towards the ultimate conservative difference scheme. II. Monotonicity and conservation combined in a second-order scheme*, J. Comput. Phys. **14** (1974), no. 4, 361-370.

[76]   —, *Towards the ultimate conservative difference scheme. V. A second-order sequel to Godunov's method*, J. Comput. Phys. **32** (1979), 101-136.

[77]   J. A. C. Weideman, *Computing the dynamics of complex singularities of nonlinear PDEs*, SIAM J. Appl. Dyn. Syst. **2** (2003), no. 2, 171-186 (electronic).

Russel E. Caflisch
Mathematics Department
University of California at Los Angeles
Los Angeles, CA 90036, United States
e-mail: rcaflisch@ipam.ucla.edu

Francesco Gargano
Marco Sammartino
Vincenzo Sciacca
Dipartimento di Matematica
Università di Palermo
90123 Palermo, Italy
e-mail: francesco.gargano@unipa.it
e-mail: marcomarialuigi.sammartino@unipa.it
e-mail: vincenzo.sciacca@unipa.it